

This is a pre print version of the following article:

Electronic and Optical Properties of Silicon Nanocrystals / C., Bulutay; Ossicini, Stefano. - STAMPA. - (2010), pp. 5-42. [10.1002/9783527629954.ch2]

Wiley-VCH Verlag GmbH & Co. KGaA
Terms of use:

The terms and conditions for the reuse of this version of the manuscript are specified in the publishing policy. For all terms of use and more information see the publisher's website.

18/12/2025 18:59

Ceyhun Bulutay¹ and Stefano Ossicini²

¹*Department of Physics, Bilkent University, Bilkent, Ankara 06800, Turkey*

²*CNR-INFM-S³ and Dipartimento di Scienze e Metodi dell'Ingegneria, Università di Modena e Reggio Emilia, via Amendola 2 Pad. Morselli, I-42100 Reggio Emilia, Italy.*

The previous decades repeatedly witnessed claims that silicon would be sidelined by various alternative material systems. In the long run, none of these claims turned out to be the case. Taking into account the changing societal and technological needs, there are strong indications that the nanocrystalline form of silicon will provide a critical support to sustain this domination as the all-purpose material of choice. The purpose of this study is to offer a comprehensive theoretical overview of the electronic structure and optical properties of Si nanocrystals (Si NCs). Starting with small NCs, we use a first-principles methodology taking into account the structural relaxations. We go beyond the one-particle approach including the self-energy corrections, by means of the GW approximation, and the excitonic effects, through the solution of the Bethe-Salpeter equation. This new approach, where many-body effects are combined with a study of the structural distortion due to the impurity atoms in the excited state, allows to calculate accurately the Stokes shift between absorption and photoluminescence spectra. Regarding the interface and impurity effects, first, the hydrogenated Si NCs are considered, followed by the discussion of oxidation, and of (co-)doping and finally, of the crystalline as well as amorphous embedding matrix. For the larger Si NCs embedded in a wide band-gap matrix containing of the order of 10,000's of atoms, an atomistic semi-empirical pseudopotential approach is utilized. A validation of the semi-empirical results is given by comparing with the experimental and first-principles data on the effective optical gap and the radiative lifetime. The linear optical absorption properties are discussed for interband, intraband and excited-state configurations. Next, third-order nonlinear optical susceptibilities are computed with full wavelength dependence and their size-scaling trends are identified. Finally, the quantum-confined Stark effect in Si NCs is analysed which reveals the discrepancy of the Stark shifts of the valence and conduction states.

I. INTRODUCTION

Several strategies have been researched over the last years for light generation and amplification in silicon. One of the most promising is based on silicon nanocrystals (Si NCs) with the idea of taking advantage of the reduced dimensionality of the nanocrystalline phase (1-5 nm in size) where quantum confinement, band folding and surface effects play a crucial role.^{1,2} Indeed, it has been found that the Si NC band-gap increases with decreasing size and a photoluminescence external efficiency in excess of 23% has been obtained.³ Si NC based LED with high efficiency have been obtained by using Si NC active layers⁴ and achieving separate injection of electrons and holes.⁵ Moreover, optical gain under optical pumping has been already demonstrated in a large variety of experimental conditions.⁶⁻¹¹

After the initial impulse given by the pioneering work of Canham on photoluminescence (PL) from porous Si,¹² nanostructured silicon has received extensive attention. This activity is mainly centered on the possibility of getting relevant optoelectronic properties from nanocrystalline Si. The huge efforts made towards matter manipulation at the nanometer scale have been motivated by the fact that desirable properties can be generated just by changing the system dimension and shape. Investigation of phenomena such as the Stokes shift (difference between absorption and emission energies), the PL emission energy vs nanocrystals size, the doping properties, the radiative lifetimes, the non-linear optical properties, the quantum-confined Stark effect etc. can give a fundamental contribution to the understanding of how the optical response of such systems can be tuned. An interesting amount of work has been done regarding excited Si NCs,^{2,13-23} but a clear comprehension of some aspects is still lacking. The question of surface effects, in particular oxidation, has been addressed in the last years. Both theoretical calculations and experimental observations have been applied to investigate the possible active role of the interface on the optoelectronic properties of Si NCs. Different models have been proposed: Baierle *et al.*²⁴ have considered the role of the surface geometry distortion of small hydrogenated Si clusters in the excited state. Wolkin *et al.*²⁵ have observed that oxidation introduces defects in the Si NC band-gap which pin the transition energy. They claimed the formation of a Si=O double bond as the pinning state. The same conclusion has been recently reached by other authors,²⁶⁻²⁹ whereas Vasiliev *et al.*³⁰ have pointed out that similar results can be obtained also for O connecting two Si atoms (single bond) at the Si NC surface. The optical gain observed in Si NC embedded in SiO₂ has given a further impulse to these studies. Interface radiative states have been suggested to play a key role in the mechanism of population inversion at the origin of the gain.^{6,8,31} Thus the study of the nature and the properties of the interface between the Si NC and the SiO₂ host matrix has become crucial.

The calculation of the electronic and optical properties of nanostructures is a difficult task. First-principle studies are very demanding and in order to investigate very large systems empirical methods are needed. In this paper we present and resume a comprehensive study of the structural, electronic and optical properties of undoped and doped Si nanostructures terminated by different interfaces and, in particular, embedded in silicon dioxide matrix. For smaller nanocrystals we will present *ab initio* results, in particular the absorption and emission spectra and the effects induced by the creation of an electron-hole pair are calculated and discussed in detail including many-body effects. The aim is to investigate in a systematic way the structural, electronic and stability properties of silicon nanostructures as a function of size and capping species well as pointing out the main changes induced by the nanostructure excitation.

The indisputable superiority of the first-principles approaches is gloomed by their applicability to systems of less than a thousand atoms with the current computer power. On the other hand, fabricated NCs of sizes 2-5 nm embedded in an insulating host matrix require computationally more feasible techniques that can handle more than 10,000 atoms including the surrounding matrix atoms. There exist several viable computational approaches for low-dimensional structures with a modest computational budget. The most common ones are the envelope function $\mathbf{k}\cdot\mathbf{p}$,³² semi-empirical tight-binding,³³ and semi-empirical pseudopotential techniques.³⁴ The decision of which one to use should be made according to the accuracy demands, but a subjective dimension is also brought by the established biases of the particular practitioners. As the simplest of all, the envelope function $\mathbf{k}\cdot\mathbf{p}$ approach lacks the atomistic touch and more importantly, both qualitative and significant quantitative errors were identified mainly derived from the states that were not accounted by the multiband $\mathbf{k}\cdot\mathbf{p}$ Hamiltonian.³⁵ As an atomistic alternative, the semi-empirical tight binding approach has been successfully employed by several groups; see, Ref. 33 and references therein. Its traditional rival has always been the semi-empirical pseudopotential approach. About a decade ago, Wang and Zunger proposed a more powerful technique that solves the pseudopotential-based Hamiltonian using a basis set formed by the linear combination of bulk bands of the constituents of the nanostructure.^{36,37} Its main virtue is that it enables an insightful choice of a basis set with moderate number of elements. It should be mentioned that, the idea of using bulk Bloch states in confined systems goes back to earlier times; one of its first implementations being the studies of Ninno *et al.*^{38,39} Up to now, it has been tested on self-assembled quantum dots,^{36,37} superlattices,^{40,41} and high-electron mobility transistors.⁴² In the context of Si NCs, very recently it has been used for studying the effects of NC aggregation,⁴³ the linear,⁴⁴ and third-order nonlinear optical properties,⁴⁵ and also for characterizing the Auger recombination and carrier multiplication.⁴⁶ The fact that it is a pseudopotential-based method makes it more preferable over the empirical tight binding technique for the study of *optical* properties. For these reasons, in the case of large NCs, we shall make use of the linear combination of bulk bands technique. For both small NCs analysed with *ab initio* techniques, and larger NCs dealt with atomistic semi-empirical approaches, a comparison with the experimental outcomes will be presented and discussed, whenever possible.

The organization of this review is based on two main sections for discussing the methodology and results of small and large NCs. A description of the theoretical methods used in the *ab initio* calculations is given in Sec. II. The first-principle study of the physical systems is then presented starting from the analysis of hydrogenated Si NC (Sec. II A). We then consider the effect of oxidation (Sec. II B), of doping (Sec. II C) and finally of an embedding matrix (Sec. II D). As for the larger NCs embedded in a wide band-gap matrix, in Sec. III, first a theoretical framework of the semi-empirical approach is presented. Next, the comparisons of our results for the case of effective optical gap (Sec. III A), and radiative lifetime (Sec. III B) are presented. This is followed by the linear optical absorption properties (Sec. III C), where our interband, intraband and excited-state absorption results are summarized. The important subject of third-order nonlinear optical susceptibility is discussed in Sec. III D. Finally, a theoretical analysis of the quantum-confined Stark effect in Si NCs is offered in Sec. III E.

II. ELECTRONIC STRUCTURE AND OPTICAL PROPERTIES FOR SMALL NANOCRYSTALS: *AB INITIO* CALCULATION

The results have been obtained through plane-wave, pseudopotential density functional (DFT) calculations. In the case of the H-Si NC (see Sec. II A) all the calculations have been performed with the ABINIT code.⁴⁷ Norm-conserving, non-local Hamann-type pseudopotentials have been used. The Kohn-Sham wave functions have been expanded within a plane-wave basis set, choosing an energy cutoff of 32 Ry. The calculations performed are not spin-polarized. Each H-Si NC has been embedded within a large cubic supercell, containing vacuum in order to make nanocrystal-nanocrystal interactions negligible. The calculations for each cluster have been performed both in ground and excited state. Full relaxation with respect to the atomic positions is performed for all the considered systems. We have addressed the issue of excited state configurations, which is mostly relevant for Si NC with a high surface-to-volume ratio using the so called Δ -SCF method,⁴⁸⁻⁵¹ where total energies are calculated both in the ground state (GS) and in the excited state (ES). Here the ES corresponds to the electronic configuration in which the highest occupied single-particle state [highest occupied molecular orbital (HOMO)] contains a hole, while the lowest unoccupied single-particle state [lowest

unoccupied molecular orbital (LUMO)] contains the corresponding electron. Thus, one can extract the absorption and emission energies and through their difference calculate the Stokes or Frank-Condon shift due to the lattice relaxation induced by the electronic excitation.

For the oxidized and doped Si NCs (see Sec. IIB and Sec.IIC) all the DFT calculations have been performed using the ESPRESSO package,⁵² within the generalized gradient approximation (GGA) using Vanderbilt ultrasoft⁵³ pseudopotentials for the determination of the structural properties and norm-conserving pseudopotential within the local density Approximation (LDA) at the optimized geometry to evaluate the electronic and optical properties. This choice is due to the fact that Vanderbilt ultrasoft pseudopotentials allow the treatment of several hundreds of atoms per unit cell in the atomic relaxation process but the lift of the norm-conservation condition is a crucial and well known problem for the calculation of the optical transition matrix elements. The Si NC have been embedded in large supercells in order to prevent interactions between the periodic replicas (about 6 Å of vacuum separates neighbor clusters in all the considered systems). A careful analysis has been performed on the convergence of the structural and electronic properties with respect to both the supercell side and plane-wave basis set cut-off. Since our aim is to allow a direct comparison between experimental data and theoretical results, we have calculate not only the transition energies within the Δ -SCF approach but also directly the absorption and emission optical spectra. The excited state corresponds to the electronic configuration in which the highest occupied single-particle state (HOMO) contains a hole, while the lowest unoccupied single-particle state (LUMO) contains the corresponding electron. The optical response of the nanocrystal has been evaluated for both the ground and the excited state optimized geometries through the imaginary part of the dielectric function $\epsilon_2(\omega)$

$$\epsilon_2^\alpha(\omega) = \frac{4\pi^2 e^2}{m^2 \omega^2} \sum_{v,c,k} \frac{2}{V} |\langle \psi_{c,k} | p_\alpha | \psi_{v,k} \rangle|^2 \delta[E_c(k) - E_v(k) - \hbar\omega] \quad (1)$$

where $\alpha = (x, y, z)$, E_v and E_c denote the energies of the valence $\psi_{v,k}$ and conduction $\psi_{c,k}$ band states at a k point (Γ in our case), and V is the supercell volume. Owing to the strong confinement effects, only transitions at the Γ point have been considered. In order to perform emission spectra calculations, we have used the excited state geometry and the ground state electronic configuration. Thus, strictly speaking, $\epsilon_2(\omega)$ corresponds to an absorption spectrum in the new structural geometry of the excited state: in this way we are simply considering the emission, in a first approximation, as the time reversal of the absorption⁵⁴ and therefore as a sort of photoluminescence spectra of the nanocrystals. Moreover in several cases we go beyond the one-particle approach including the self-energy corrections, by means of the GW approximation,⁵⁵ and the excitonic effects, through the solution of the Bethe-Salpeter equation (BSE).⁵⁶ To take into account the inhomogeneity of the system local fields effects (LF) have been considered, too. This new approach where many-body effects, such as the self-energy corrections and the hole-electron interaction, are combined with a study of the structural distortion due to the impurity atoms in the excited state, allows to calculate accurately the Stokes shift between absorption and photoluminescence spectra.

A. Hydrogenated Silicon Nanocrystals

In this section we present an analysis of the structural, electronic and optical properties of hydrogenated silicon nanocrystals (H-Si NCs) as a function of size and symmetry and in particular we will point out the main changes induced by the nanocrystal excitation. The calculations for each cluster have been performed both in ground and excited state. The starting configuration for each cluster has been fixed with all Si atoms occupying the same position as in the bulk crystal, and passivating the surface with H atoms placed along the bulk crystal directions, at a distance determined by studying the SiH₄ molecule. It is worth pointing out that the starting H-Si NC has T_d symmetry, which is kept during relaxation in the ground state configuration. Nevertheless for excited state configurations such symmetry is generally lost, due to the occupation of excited energy levels. We have first of all investigated the structural distortions caused by the relaxation of these structures in different electronic configurations. The analysis of the structural properties reveals that the average Si-Si bond approaches the bulk bond length as the cluster dimension increases. In particular, moving from the center of the cluster toward the surface, a contraction of the outer Si shells is observed. The presence of a electron-hole pair in the clusters causes a strong deformation of the structures with respect to their ground-state configuration, and this is more evident for smaller systems and at the surface of the H-Si NC. This is what we expect, since for large clusters the charge density perturbation is distributed throughout all the structure, and the effect it locally induces becomes less evident. Baierle *et al.*²⁴ and G. Allan *et al.*⁵⁷ stressed the importance of bond distortion at the Si NC surface in the excited state (ES) in creating an intrinsic localized state responsible of the PL emission. The structural analysis is immediately reflected into the electronic structure. It can be noted from table I the expected decrease of the energy gap on increasing the cluster dimension and also that the excitation of the electron-hole pair causes a reduction of the energy gap as much significant as smaller is

the cluster. For small excited clusters the HOMO and LUMO become strongly localized in correspondence of the distortion, giving rise to defect-like states which reduce the gap. The distortion induced by the nanocluster excitation can give a possible explanation of the observed Stokes shift in these systems. The radiation absorption of the cluster in its ground state configuration induces a transition between the HOMO and LUMO levels, which for all these clusters is optically allowed. Such a transition is followed by a cluster relaxation in the excited state configuration giving rise to distorted geometries (as previously shown) and to new LUMO and HOMO, whose energy difference is smaller than that in the ground-state geometry. It is between these two last states that emission occurs, thus explaining the Stokes shift. It is also worth pointing out how such a shift changes as a function of the dimension. Being the distortion smaller for larger clusters, it is expected that the Stokes shift decreases on increasing the dimension. This is shown in table I where the absorption and emission energies together with the Stokes Shift calculated as described in section II are reported.

TABLE I: Calculated values for the ground (GS) and excited (EXC) state HOMO-LUMO energy gaps and for the absorption and emission energies calculated within the Δ -SCF approach for the considered H-Si NC. All values are in eV.

	Absorption	GS HOMO- LUMO gap	Emission	EXC HOMO- LUMO gap
Si₁H₄	8.76	7.93	0.38	1.84
Si₅H₁₂	6.09	5.75	0.42	0.46
Si₁₀H₁₆	4.81	4.71	0.41	0.55
Si₂₉H₃₆	3.65	3.58	2.29	2.44
Si₃₅H₃₆	3.56	3.50	2.64	2.74

A number of papers present in literature consider the HOMO-LUMO gaps of the ground and excited state as the proper absorption and emission energies; this leads to wrong results, mostly for the smaller clusters. In fact, from Table I it is clearly seen that the smaller the H-Si NC, the larger is the difference between the absorption and HOMO-LUMO ground-state (GS) gap and between emission and HOMO-LUMO excited-state (EXC) gap. In our calculations, on going from smaller to larger clusters the difference between the HOMO-LUMO gap in the ground state and the absorption gap becomes smaller. In particular the GS HOMO-LUMO gap tends to be smaller than the absorption energy while the EXC HOMO-LUMO gap tends to be larger than the emission energy. In conclusion, trying to deduce the Stokes Shift simply from the HOMO-LUMO gaps leads to errors especially for small clusters. In particular the GS HOMO-LUMO gap tends to be smaller than the absorption energy while the EXC HOMO-LUMO gap tends to be larger than the emission energy. In conclusion, trying to deduce the Stokes shift simply from the HOMO-LUMO gaps leads to not negligible errors which are more significant for smaller clusters. When comparing our results for the ground state with other DFT calculations we note that there is in general a good agreement between them. It is worth mentioning that our results for the absorption gaps of the Si₁H₄ (8.76 eV) and Si₅H₁₂ (6.09 eV) clusters agree quite well with the experimental results of Itoh *et al.*⁵⁸ They have found excitation energies of 8.8 eV and 6.5 eV respectively. Regarding the Stokes shift, really few data exist in literature, and, in particular for really small H-Si NC (from Si₁H₄ to Si₁₀H₁₆), no data exist. The dependence of the Stokes shift from the H-Si NC size qualitatively agrees with the calculations of Puzder *et al.*⁴⁸ and Franceschetti *et al.*⁴⁹

B. Oxidized Silicon Nanocrystals

Recent experimental data have shown a strong evidence that the surface changes of silicon nanocrystals exposed to oxygen produce substantial impact on their optoelectronics properties, thus oxidation at the surface has to be taken into account. In this section we will analyze the optical properties of oxidized Si NCs first of all, using the Δ -SCF method.^{48–51} Each Si NC has been embedded within a large cubic supercell, containing vacuum in order to make nanocrystal-nanocrystal interactions negligible. The starting configuration for each cluster has been fixed with all Si atoms occupying the same position as in the bulk crystal, and passivating the surface with H atoms placed along the bulk crystal directions, at a distance determined by studying the SiH₄ molecule. Two classes of systems have been studied, the Si₁₀ and the Si₂₉ core based nanoclusters, and three type of Si/O bonds as been introduced at the cluster surface: the Si-O back bond, the Si> O bridge and the Si=O double bond. Through formation energy calculation we have found that the configuration with the back-bonded oxygen is not favored with respect to the other two and moreover the bridge bonded configuration has been demonstrated to lead to the stablest isomer configuration,^{59,60} too. Full relaxation with respect to the atomic positions is performed within DFT limit for all systems both in the ground and excited configurations using norm conserving LDA pseudopotential with an energy cutoff of 60 Ry.⁵²

The ionic relaxation has produced structural changes with respect to the initial geometry which strongly depend on the type of surface termination. In the case of $\text{Si}_{10}\text{H}_{14}=\text{O}$, the changes are mainly localized near the O atom, in particular the angle between the double bonded O and its linked Si atom is modified. In the bridge structure, instead, the deformation is localized around the Si-O-Si bond determining a considerable strain in the Si-Si dimer distances.⁶⁰ Similar results are obtained for the larger Si_{29} based clusters. The only difference is that now the distortion induced by the promotion of an electron is smaller, as expected, since for larger clusters the charge density perturbation is distributed throughout the structure, and the effect locally induced becomes less evident. These structural changes are reflected in the electronic and optical properties.

In Table II absorption and emission gaps are reported: the red shift of the emission gap with respect to the absorption is less evident for the case of the cluster with the double-bonded oxygen (see the Stokes shift values); the same can be observed for the double-bonded $\text{Si}_{29}\text{H}_{34}\text{O}$.

TABLE II: Absorption and emission energy gaps and Stokes shift calculated as total energy differences within the Δ -SCF approach. All values are in eV.

	Absorption	Emission	Stokes shift
$\text{Si}_{10}\text{H}_{14}=\text{O}$	2.79	1.09	1.70
$\text{Si}_{10}\text{H}_{14} > \text{O}$	4.03	0.13	3.90
$\text{Si}_{29}\text{H}_{34}=\text{O}$	2.82	1.17	1.65
$\text{Si}_{29}\text{H}_{34} > \text{O}$	3.29	3.01	0.28

The oxygen double-bonded seems hence almost size independent: actually, the presence of this kind of bond creates localized states within the gap that are not affected by quantum confinement as previously predicted.⁶¹

As already stated in Sec. II we have calculated not only the transition energies within the Δ -SCF approach but also directly the absorption and emission optical spectra. Actually, for both the calculated GS and ES optimized geometry, we have evaluated the optical response through first-principles calculations also beyond the one-particle approach. We have considered the self-energy corrections by means of the GW method and the excitonic effects through the solution of the Bethe-Salpeter equation. The effect of the local fields is also included. In Table III, the calculated gaps at different levels of approximation (DFT-LDA, GW and BS-LF approaches) are reported for both the Si_{10} and Si_{29} based nanocrystals.

The main result common to absorption and emission is the opening of the LDA band-gap with the GW corrections by amounts weakly dependent on the surface termination but much larger than the corresponding 0.6 eV of the Si bulk case. Looking at the BS-LF calculations, we note a sort of compensation (more evident in the GS than in the ES) of the self-energy and excitonic contributions: the BS-LF values return similar to the LDA ones. The only exception are the BS-LF calculations for the excited state geometries of the clusters with Si-O-Si bridge bonds at the surface. Concerning the differences between the values of the Stokes shifts calculated through the Δ -SCF approach in Table II or through the MBPT in Table III they are essentially due to the ability or not of the two methods of distinguish dark transitions. In the MBPT the oscillator strengths of each transition are known while the Δ -SCF approach only gives the possibility to find the energy of the first excitation: if this transition is dark (and the Δ -SCF approach do not give this information) the associated energy is not the real optical gap. A clearer insight on the MBPT results is offered by Fig. 1 (left panel), where the calculated absorption and emission spectra for all the oxidized Si_{10} based clusters are depicted and compared with the fully hydrogenated cluster. Self-energy, local-field and excitonic effects (BS-LF) are fully taken into account. Concerning the absorption spectra (Fig. 1, dashed lines), all three cases show a similar smooth increase in the absorption features. Different is the situation for the emission related spectra (Fig. 1, solid lines). Here, whereas the situation remain similar for the fully hydrogenated $\text{Si}_{10}\text{H}_{16}$ (top panel) cluster and for the $\text{Si}_{10}\text{H}_{14}=\text{O}$ (central panel) cluster, in the case of a Si-O-Si bridge bond (Fig. 1 (bottom panel)) an important

TABLE III: Absorption and emission gaps calculated as HOMO-LUMO differences within DFT-LDA and GW approaches and as the lowest excitation energy when excitonic and local field effects (BS-LF) are included. In the last column the Stokes shift calculated in the BS-LF approximation is reported. In parenthesis also the lowest dark transitions (when present) are given. All values are in eV.

	Absorption			Emission			Stokes shift
	LDA	GW	BS-LF	LDA	GW	BS-LF	
$\text{Si}_{10}\text{H}_{14}=\text{O}$	3.3 (2.5)	7.3 (6.5)	3.7 (2.7)	0.8	4.6	1.0	2.7
$\text{Si}_{10}\text{H}_{14} > \text{O}$	3.4	7.6	4.0	0.1	3.5	1.5	2.5
$\text{Si}_{29}\text{H}_{34}=\text{O}$	2.5	6.0	3.7 (3.1)	0.9	4.1	1.2	2.5
$\text{Si}_{29}\text{H}_{34} > \text{O}$	2.3	4.8	2.3	0.4	3.0	2.2 (0.3)	0.1

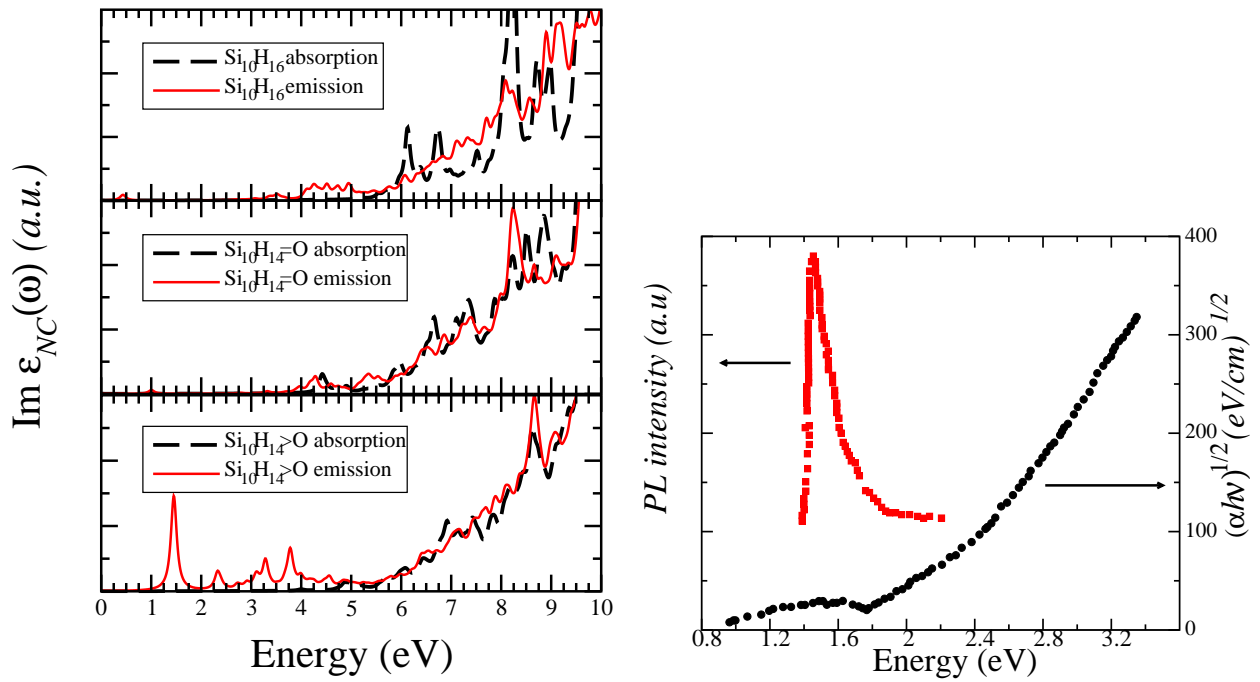


FIG. 1: Emission (solid line) and absorption (dashed line) spectra: imaginary part of the dielectric function for the three considered Si NC. On the left: $\text{Si}_{10}\text{H}_{16}$ (top panel), $\text{Si}_{10}\text{H}_{14}=\text{O}$ (central panel) and $\text{Si}_{10}\text{H}_{14}>\text{O}$ (bottom panel). On the right: experimental results for emission (red curve on the left) and absorption (on the right) by Ref. 62.

excitonic peak, separated from the rest of the spectrum, is evident at 1.5 eV. Actually bound excitons are present also in the fully hydrogenated (at 0.4 eV) and in the $\text{Si}_{10}\text{H}_{14}=\text{O}$ (at 1.0 eV) clusters, nevertheless, the related transitions are almost dark and the emission intensity is very low. Only in the case of the Si-O-Si bridge bond a clear PL peak appears thanks to the strong oscillator strength of the related transition. The right panel of Fig. 1 shows the experimental absorption and emission spectra measured by Ma *et al.*⁶² for Si-nanodots embedded in SiO_2 matrix. A strong photoluminescence peak appears around 1.5 eV. Comparison of the experimental spectra with our results suggest that the presence of a Si-O-Si bridge bond at the surface of Si NC and the relative deformation localized around the Si-O-Si bond can explain the nature of luminescence in Si nanocrystallites: only in this case the presence of an excitonic peak in the emission related spectra, red shifted with respect to the absorption onset, provides an explanation for both the observed SS and the near-visible PL in Si NC. Similar results have been obtained in the case of Si_{29} -based clusters. Only in the case of O in bridge position there is a cage distortion at the interface that allows the presence of significant emission features in the optical region.

C. Doped Silicon Nanocrystals

1. Single-doped Silicon Nanocrystals

We resume here the effects of size and shape of Si NCs on the incorporation of group-III (B and Al), group-IV (C and Ge), and group-V (N and P) impurities. Single-doping has been investigated both in spherical and faceted-like Si NCs.^{63,64} The spherical Si NC are built taking all the bulk Si atoms contained within a sphere of a given radius and terminating the surface dangling bonds with H; whereas the faceted Si NCs are resulting from a shell-by-shell construction procedure which starts from a central atom and adds shells of atoms successively. Spherical-like Si NCs are the $\text{Si}_{29}\text{H}_{36}$, $\text{Si}_{87}\text{H}_{76}$, $\text{Si}_{147}\text{H}_{100}$, and $\text{Si}_{293}\text{H}_{172}$ clusters and the faceted Si NCs are the Si_5H_{12} , $\text{Si}_{17}\text{H}_{36}$, $\text{Si}_{41}\text{H}_{60}$, and $\text{Si}_{147}\text{H}_{148}$ clusters. The average diameter of doped and undoped Si NCs after relaxation is about 2.3 nm for the largest crystal considered. The substitutional impurity site is the one of the Si atom at the center of the NC. As for impurities in bulk Si, Jahn- Teller distortions occur in the neighborhood of the impurity sites and the bond lengths show a dependence with respect to size and shape of the Si NCs. After ionic relaxation the Si-X bond lengths ($X=\text{B}$, Al, C, Ge, N, and P) tend to be longer for faceted than for spherical-like Si NCs. A little variation

of the impurity levels with respect to the shape of the Si NCs is observed. Boron and aluminum give rise to shallow acceptor levels, whereas phosphorus gives rise to shallow donor level and nitrogen to a deep donor level. The energetic positions of the impurity levels become deeper as the size of the Si NC decreases and tend nearly to the position of the corresponding impurity levels of Si bulk as the size of the Si NC increases. For all the impurities considered the lowest-energy transitions occur at lower energies than the ones in the corresponding undoped Si NCs. The optical absorption spectra of medium and large doped Si NCs exhibit an onset of absorption characteristic of indirect-gap materials. High peaks in the spectra can be found in the Si NCs whose diameters are smaller than 1.0 nm. Moreover the radiative lifetimes are sensibly influenced by the shape, especially for the small Si NCs, whereas these influences disappear when the size of the nanoparticles increase.

Starting from the Si_nH_m nanocluster,⁵¹ the formation energy (FE) for the neutral X impurity can be defined as the energy needed to insert the X atom with chemical potential μ_X within the cluster after removing a Si atom (transferred to the chemical reservoir, assumed to be bulk Si)

$$E_f = E(\text{Si}_{n-1}\text{XH}_m) - E(\text{Si}_n\text{H}_m) + \mu_{\text{Si}} - \mu_X. \quad (2)$$

Here E is the total energy of the system, μ_{Si} the total energy per atom of bulk Si, μ_X the total energy per atom of the impurity. The results show that for smaller Si-MCs a larger energy is needed for the formation of the impurity. There is a slight tendency in formation energy that suggests that the incorporation of the impurities is more favored in spherical than in faceted Si NCs. This tendency is not valid for the neutral Ge and P impurities, which present a formation energy nearly independent of the shape, and by the Al impurity, for which the incorporation is slightly favored for faceted Si NCs. We have also calculated how the FE changes as a function of the impurity position within the Si NC.⁶³ For the B neutral impurity in the large $\text{Si}_{146}\text{BH}_{100}$ cluster we have moved the impurity from the cluster center toward the surface along different paths still considering substitutional sites. It comes out that as far as the internal core is concerned, variations not higher than 0.06 eV are found. On the contrary, an energy drop between 0.25 and 0.35 eV is found as the B impurity is moved to the Si layer just below the surface. This is explained by considering that such positions are the only ones which allow a significant atomic relaxation around the impurity, because in the other cases the surrounding Si cage is quite stable. Thus, as the B atom is moved toward the surface the FE decreases, making the subsurface positions more stable.

2. Co-doped Silicon Nanocrystals

As already said simultaneous doping with n - and p -type impurities represent a way to overcome the low radiative recombination efficiency in our systems so, starting from the already described hydrogenated Si NCs and following the work of Fujii *et al.*,⁶⁵ we have doped the $\text{Si}_{35}\text{H}_{36}$ cluster locating the B and P impurities in substitutional positions just below the nanocrystal surface. It is worth mentioning that this arrangement represents the most stable configuration, as confirmed by theoretical and experimental works.^{66–68} Full relaxation with respect to the atomic positions has been allowed and electronic properties have been computed through DFT calculations. We have found that in all the case of co-doping the formation energy is strongly reduced, favoring this process with respect to the single doping. The choice of studying the small $\text{Si}_{33}\text{BPH}_{36}$ cluster (see Fig. 3) (diameter around 1 nm) is due to the fact that the GW-BSE calculation,⁶⁹ necessary to obtain the optical spectra, are very computing demanding. The energy levels of this system at the Γ point calculated at the optimized geometries are shown in Figure 2 where only the levels corresponding to the HOMO, LUMO, HOMO-1 and LUMO+1 states are depicted. Calculated square modulus contour plots related to HOMO and LUMO states, have shown their localization within the Si NC, in particular the HOMO state is localized on the B impurity while the LUMO is localized on the P one. The presence of these donor and acceptor states lowers the energy gap from 3.51 eV for the pure cluster to 2.86 eV for the doped one. In principle, starting with a bigger cluster, for which the energy gap is smaller than in this case, it is possible through codoping to tune the gap also below the bulk Si band gap as experimentally observed by Fuji and coworkers.⁷⁰ In order to give a complete description, within the many-body framework, of the codoped Si NC response to an optical excitation, we consider both the self-energy corrections by means of the GW method⁷¹ to obtain the quasiparticle energies and the excitonic effects through the solution of the Bethe-Salpeter equation. The effect of local fields is also included, to take into account the inhomogeneity of the systems. To carry out emission spectra calculations, we have used the excited state geometry and the ground state electronic configuration as already described in section II. Thus, the electron-hole interaction is here considered also in the emission geometry. Fig.4 (right panel) shows the calculated absorption and emission spectra fully including the many-body effects. The electron-hole interaction yields significant variations with respect to the single-particle spectra (shown in the left panel), with an important transfer of the oscillator strength to the low energy side. Moreover, in the emission spectrum the rich structure of states characterized, in the low energy side, by the presence of excitons with largely different oscillator strengths, determines excitonic gaps well below the optical absorption onset. Thus the calculated emission spectrum results to be red shifted to lower energy with respect

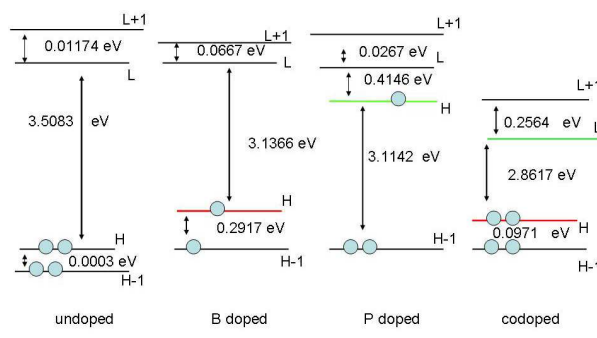


FIG. 2: Calculated energy levels at Γ point for the $\text{Si}_{33}\text{BPH}_{36}\text{-NC}$. Alignment has been performed locating at the same energy the fully occupied levels with the same type of localization.

to the absorption one. This energy difference between emission and absorption, the Stokes shift, can be lead back to the relaxation of the Si NCs after the excitation process. The new important features that appear in the emission many-body spectra are related to the presence of both B and P impurities as showed by Fig. 5, which gives the real-space probability distribution $|\psi_{exc}(r_e, r_h)|^2$ for the bound exciton as a function of the electron position r_e when the hole is fixed in a given r_h position. In this case the hole is fixed on the boron atom and we see that the bound exciton is mainly localized around the phosphorus atom. From Table IV, it can be seen that the single-particle DFT results strongly underestimate the absorption and emission edge with respect to the GW+BSE calculation, in which the excitonic effect are taken exactly into account. This means that, in this case, the cancellation between GW gap opening (which gives the electronic gap) and BSE gap shrinking (which originates the excitonic gap) is only partial.⁷² It is also interesting to note that the calculated Stokes shifts are almost independent on the level of the computation. The difference between the GW electronic gap and the GW+BSE optical excitonic gap gives the exciton binding energy E_b . We note the presence of exciton binding energies as big as 2.2 eV, which are very large if compared with bulk Si (~ 15 meV) or with carbon nanotubes^{73,74} where $E_b \sim 1$ eV, but similar to those calculated for undoped Si NCs⁷⁵ of similar size and for Si and Ge small nanowires.^{76,77}

TABLE IV: Absorption and Emission gaps calculated as HOMO-LUMO difference through a DFT, the many-body GW and a GW-BSE approach.

$\text{Si}_{33}\text{BPH}_{36}$	DFT	GW	GW+BSE
Abs. (eV)	2.80	5.52	3.35
Ems. (eV)	1.79	4.37	2.20
Δ (eV)	1.01	1.15	1.15

It is interesting to note that the HOMO-LUMO transition in the emission spectrum at 2.20 eV is almost dark while an important excitonic peak is evident at about 2.75 eV (see Fig. 4), red-shifted with respect to the first absorption

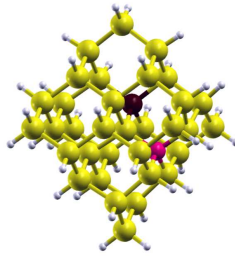


FIG. 3: Relaxed structure of the $\text{Si}_{33}\text{BPH}_{36}$ codoped nanocrystal (diameter=1.10 nm). Gray balls represent Si atoms, while the light gray balls are the hydrogens used to saturate the dangling bonds. B (dark gray) and P (black) impurities have been located at subsurface position in substitutional sites on opposite sides of the nanocrystals. The relaxed impurity distance is $\text{DBP}=3.64 \text{ \AA}$.

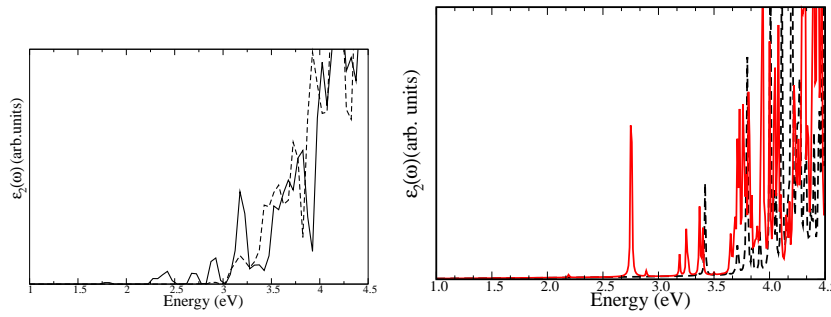


FIG. 4: Left panel: Single-particle imaginary part of the dielectric function for the codoped $\text{Si}_{33}\text{BPH}_{36}$ nanocrystal in the ground (dashed line) and excited (solid line) geometries. Right panel: absorption (dashed line) and emission (solid line) many-body spectra of $\text{Si}_{33}\text{BPH}_{36}$.

peak.

D. Silicon Nanocrystals Embedded in a SiO_2 matrix

In this section our goal is to build up a simple model to study the properties of Si nanocrystals embedded in SiO_2 matrix from a theoretical point of view.^{78,79} *Ab initio* calculations of the structural, electronic and optical properties of Si NCs embedded in a crystalline SiO_2 matrix have been carried out starting with a cubic cell ($l = 14.32 \text{ \AA}$) of SiO_2 β -cristobalite (BC).⁸⁰ The crystalline cluster has been obtained by a spherical cut-off of 12 O atoms at the center of a $\text{Si}_{64}\text{O}_{128}$ BC geometry, as shown in Fig. 6 (top panels). In this way we have built an initial supercell of 64 Si and 116 O atoms with 10 Si bonded together to form a small crystalline skeleton. No defects (dangling bonds) are present at the interface and all the O atoms at the Si NC surface are single bonded with the Si atoms of the cluster. The amorphous silica model has been generated using classical molecular dynamics simulations of quenching from a melt; the simulations have been done using semi-empirical ionic potentials,⁸¹ following a quench procedure.⁸² The amorphous dot has been obtained by a spherical cut-off of 10 O atoms from a $\text{Si}_{64}\text{O}_{128}$ amorphous silica cell, as shown in Fig. 6 (bottom panels). For both the crystalline and amorphous case we have performed successive *ab initio* dynamics relaxations with the SIESTA code⁸³ using Troullier-Martins pseudopotentials with non-local corrections, and a mesh cutoff of 150 Ry. No external pressure or stress were applied and we left all the atom positions and the cell dimensions totally free to move.

Electronic and optical properties of the relaxed structures have been calculated in the framework of DFT, using the ESPRESSO package.⁵² Modification of the band structure and of the absorption spectrum due to the many-body effects have been also computed.

In parallel to the design of the $\text{Si}_{10}/\text{SiO}_2$ system, both crystalline and amorphous, we have studied three other systems; i) the pure matrix (SiO_2) (the BC for the crystalline case and the glass for the amorphous one), ii) the isolated Si NC extracted by the nc-silica complex (both crystalline and amorphous) relaxed structure and capped by hydrogen atoms ($\text{Si}_{10}\text{-H}$), iii) the Si NC and the first interface oxygens extracted as in point ii), passivated

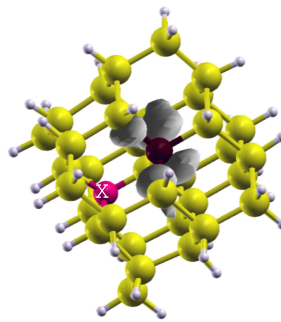


FIG. 5: Excitonic wave function of $\text{Si}_{33}\text{BPH}_{36}$ (atom colors as in Fig. 3). The gray isosurface represents the probability distribution of the electron, with the hole fixed on the B impurity.

by H atoms ($\text{Si}_{10}\text{-OH}$).⁸⁴ The goal is to separate the properties related to the Si NC from those related to the matrix in order to check the possible role of the Si NC/matrix interface, in fact the comparison of the results relative to different passivation regimes (H or OH groups) could give some insight on the role played by the interface region.

From the analysis of the relaxed crystalline $\text{Si}_{10}/\text{SiO}_2$ supercell emerges that the Si NC has a strained structure with respect to the bulk Si,⁸⁵ while the BC matrix around is strongly distorted near the Si NC and progressively reduce its stress going from the nc to the external region.^{86,87} Concerning the structure of the cluster in the amorphous glass the system (both the cluster and the matrix) has completely lost memory of the starting tetrahedral symmetry configuration. There aren't dangling bonds at the cluster surface while some bridge-bonded oxygens appear that where not present in the crystalline case.⁸⁸

Table V shows the comparison between the E_G of all the considered systems. For the crystalline case we see, first of all, a strong reduction of the $\text{Si}_{10}/\text{SiO}_2$ gap with respect to both the bulk BC SiO_2 and the isolated Si NC passivated by H atoms ; finally, as reported by Ref. 25,27–29,89,90, the passivation by OH groups tends to red-shift the energy spectrum, resulting in a gap similar to that of the embedded Si NC.

The smaller gap of the $\text{Si}_{10}/\text{SiO}_2$ system with respect to the SiO_2 BC bulk case is clearly due to the formation, at the conduction and valence band edges, of confined, flat states. These new states are not simply due to the Si NC; actually they are not present in the case of the isolate Si NC capped by H atoms, but are instead visible for the isolated Si NC passivated by OH groups. This means that a strong influence on the electronic properties of the host matrix is played not only by the presence of the Si NC but in particular by the interface region where O atoms play a crucial role. Deep inside the bands, the typical behavior of the bulk matrix is still recognizable.

Concerning the electronic properties of the amorphous systems, the E_G of the embedded Si NC and of the isolated $\text{Si}_{10}\text{-a-OH-NC}$ are similar to that of the crystalline case and, as in the crystalline case, one can find band edges states due to the interface region. However contrary to the crystalline case, the $\text{Si}_{10}\text{-a-H-NC}$ shows now a strongly reduced band gap. This difference can be addressed to the amorphization effects, indicating that in the amorphous case the localization process at the origin of the E_G lowering is mainly driven by the disorder.⁸⁸

In Fig.6 the square modulus contour plot of the HOMO (top left) and of the LUMO (top right) for the Si_{10}

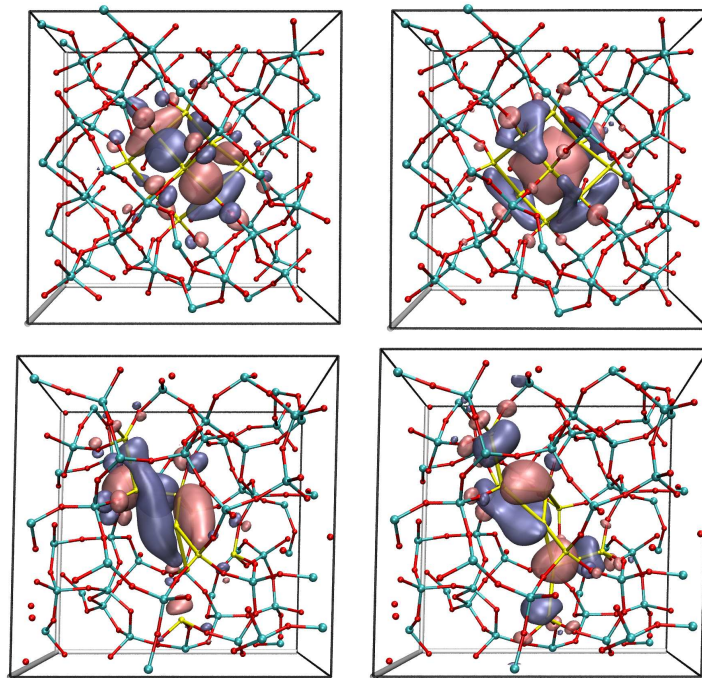


FIG. 6: Stick and ball pictures of the final optimized structure of Si_{10} in a β -cristobalite matrix (top panels) or in a SiO_2 glass (bottom panes). Dark gray spheres (red) represent O atoms, light gray (cyan) Si of the matrix and white (yellow) Si atoms of the nanocrystal. Also the isosurfaces at fixed value (7% of max. amplitude) of the square modulus $|\Psi|^2$ of HOMO (left) and LUMO (right) Kohn-Sham orbitals for the Si_{10} crystalline (top) and amorphous (bottom) clusters in the silica matrix are showed. Pink (blue) represents the positive (negative) sign of Ψ .

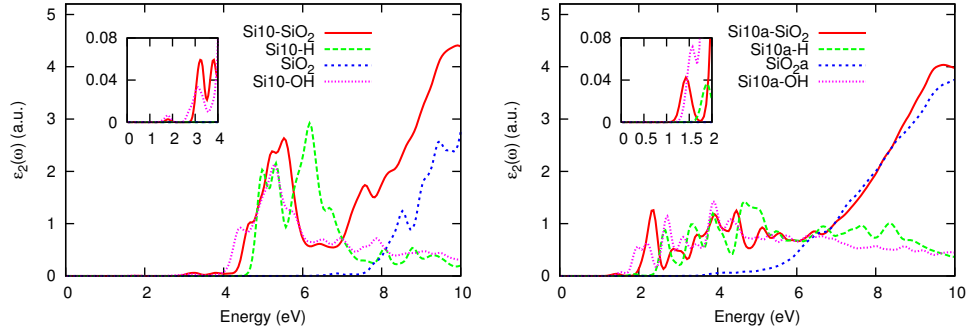


FIG. 7: Imaginary part of the dielectric function for the Si₁₀ crystalline (top) and amorphous (bottom) embedded clusters compared with that of H-terminated clusters, OH-terminated clusters and of the silica matrices. The insets show an enlargement of the spectra at low energies.

crystalline cluster in the BC matrix are reported. In both cases the spatial distribution is mainly localized on the Si NC region and on the O atoms immediately around the cluster, i.e. at the Si NC/SiO₂ interface. Also the HOMO and LUMO states for the amorphous case (reported in Fig. 6, bottom left and right) follow the shape of the Si NC, strongly deformed with respect to the ordered case. Thus they are still localized on the Si NC and on the vicinal O atoms. In our opinion, this support the important role played by the interface between the Si NC and the matrix.

The electronic properties are reflected into the optical ones. Figure 7 shows the calculated imaginary part of the dielectric function for all the structures described above. As one can see for both the crystalline and amorphous case, three regions due to the hosting matrix, to the Si NC, and to the interface, are clearly distinguishable. At high energy (> 7 eV) the spectra of the embedded Si NC resemble that of silica bulks while in the energy region between ~ 4 eV and ~ 6 eV for the crystalline and between ~ 2 eV and ~ 6 eV for the amorphous case is clear the contribution of the Si NC itself. Below these intervals, anyway, new transitions exist that are not due to the matrix alone or to the isolated, hydrogenated cluster. These low energy transitions originate from the interplay between the Si NC and the embedding matrix and in particular are also due to the O atoms present at the interface region. Indeed, comparing the imaginary part of the dielectric function (see the insets) for the embedded cluster (solid line) with that of the OH-terminated cluster (dotted line) one can see that the presence of OH groups at the surface of the cluster induce low energy transitions in fair agreement with the new peaks observed for the Si NC in the matrix. This result is in agreement with other work,⁴⁴ sustaining the idea that the deformation of the nanoclusters seems to be not determinant for the absorption onset at low energies.

The main differences between crystalline and amorphous case is related to the intensity of the peaks in the visible region (< 3 eV). Here the localization process due to the disorder enhances the intensities of the optical transitions, that in the crystalline case are very low. Many-body effects have been considered in both the crystalline and amorphous embedded Si NC. We have included quasi-particle effects within the GW approach⁵⁵ and excitonic effects within the Bethe-Salpeter equation (BSE).^{56,69}

Table VI shows the calculated E_G within DFT, GW, GW+BSE approximations. In the ordered (amorphous) case, the inclusion of GW corrections spreads up the gap of about 1.9 (1.7) eV, while the excitonic and local fields correction reduces it of about 1.5 (1.6) eV. Thus, the total correction to the LDA results to be of the order of 0.4 (0.1) eV. Now finally the E_G of the crystalline and amorphous embedded Si NC are quite different, i.e. 2.17 and 1.51 eV, respectively.

This difference is more evident looking at Fig.8 which shows a comparison of the absorption spectra for the embedded Si NC for both crystalline and amorphous case. We see that even if the inclusion of many-body effects does not change very much the situation at the onset of the absorption (see insets), it strongly depletes the intensity of the transitions in the 4-6 eV region for the crystalline case, whereas for the amorphous one the situation in the 2-6 energy region

System	SiO ₂	Si ₁₀ /SiO ₂	Si ₁₀ -OH	Si ₁₀ -H
Crystalline	5.44	1.77	1.60	4.66
Amorphous	5.40	1.41	1.55	1.87

TABLE V: Energy gap values in eV for crystalline and amorphous silica, embedded Si NC, OH-terminated Si NC, H-terminated Si NC.

Si ₁₀ /SiO ₂	DFT	GW	GW+BSE
Crystalline	1.77	3.67	2.17
Amorphous	1.41	3.11	1.51

TABLE VI: Many-body effects on the gap values (in eV) for the crystalline and amorphous embedded dots.

remain more or less the same. This is a further strong indication of the importance of localization processes for the optical properties of embedded Si NC.

Until now, no experimental measurements on Si NC with diameter of the order of 1 nm have been performed. Thus, a straightforward comparison with experimental data is not possible but the fitting of some recent measurements^{91–97} of Si NC of different sizes shows a fair agreement with our results.

III. ELECTRONIC STRUCTURE AND OPTICAL PROPERTIES FOR LARGE NANOCRYSTALS: ATOMISTIC SEMI-EMPIRICAL PSEUDOPOTENTIAL CALCULATIONS

As mentioned in the Introduction section, for large NCs, we employ the linear combination of bulk bands (LCBB) technique which makes use of the semi-empirical pseudopotentials for describing the atomistic environment. Note that we shall ignore many body effects, unlike our treatment in the previous section, where the excitonic effects were incorporated within the BSE. In this technique the NC wavefunction with a state index j is expanded in terms of the bulk Bloch bands of the constituent core and embedding medium (matrix) materials

$$\psi_j(\vec{r}) = \frac{1}{\sqrt{N}} \sum_{n,\vec{k},\sigma} C_{n,\vec{k},j}^{\sigma} e^{i\vec{k}\cdot\vec{r}} u_{n,\vec{k}}^{\sigma}(\vec{r}), \quad (3)$$

where N is the number of primitive cells within the computational supercell, $C_{n,\vec{k},j}^{\sigma}$ is the expansion coefficient set to be determined and σ is the constituent bulk material label pointing to the NC core and embedding medium. $u_{n,\vec{k}}^{\sigma}(\vec{r})$ is the cell-periodic part of the Bloch states which can be expanded in terms of the reciprocal lattice vectors $\{\vec{G}\}$ as

$$u_{n,\vec{k}}^{\sigma}(\vec{r}) = \frac{1}{\Omega_0} \sum_{\vec{G}} B_{n\vec{k}}^{\sigma}(\vec{G}) e^{i\vec{G}\cdot\vec{r}}, \quad (4)$$

where Ω_0 is the volume of the primitive cell. The atomistic Hamiltonian for the system is given by

$$\hat{H} = -\frac{\hbar^2 \nabla^2}{2m_0} + \sum_{\sigma, \vec{R}_j, \alpha} W_{\alpha}^{\sigma}(\vec{R}_j) v_{\alpha}^{\sigma}(\vec{r} - \vec{R}_j - \vec{d}_{\alpha}^{\sigma}), \quad (5)$$

where m_0 is the free electron mass, $W_{\alpha}^{\sigma}(\vec{R}_j)$ is the weight function that takes values 0 or 1 depending on the type of atom at the position $\vec{R}_j - \vec{d}_{\alpha}^{\sigma}$; an intermediate value between 0 and 1 can be used for the alloys or modeling the

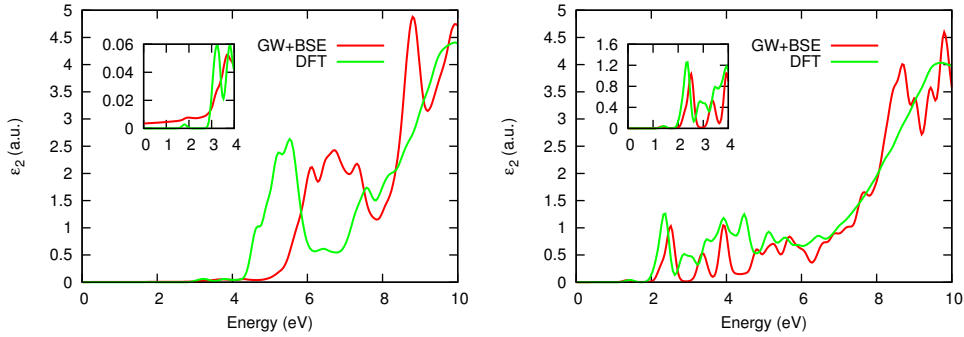


FIG. 8: DFT and GW+BSE calculated imaginary part of the dielectric function for crystalline (top) and amorphous (bottom) case.

interface region. v_α^σ is the screened spherical pseudopotential of atom α of the material σ . We use semiempirical pseudopotentials for Si developed particularly for strained Si/Ge superlattices which reproduces a large variety of measured physical data such as bulk band structures, deformation potentials, electron-phonon matrix elements, and heterostructure valence band offsets.⁹⁸ With such a choice, this approach benefits from the empirical pseudopotential method, which in addition to its simplicity has another advantage over the more accurate density functional *ab initio* techniques that run into well-known band-gap problem⁹⁹ which is a disadvantage for the correct prediction of the excitation energies.

The formulation can be cast into the following generalized eigenvalue equation:^{37,42}

$$\sum_{n,\vec{k},\sigma} H_{n'\vec{k}'\sigma',n\vec{k}\sigma} C_{n,\vec{k}}^\sigma = E \sum_{n,\vec{k},\sigma} S_{n'\vec{k}'\sigma',n\vec{k}\sigma} C_{n,\vec{k}}^\sigma, \quad (6)$$

where

$$H_{n'\vec{k}'\sigma',n\vec{k}\sigma} \equiv \langle n'\vec{k}'\sigma' | \hat{T} + \hat{V}_{\text{xtal}} | n\vec{k}\sigma \rangle,$$

$$\langle n'\vec{k}'\sigma' | \hat{T} | n\vec{k}\sigma \rangle = \delta_{\vec{k}',\vec{k}} \sum_{\vec{G}} \frac{\hbar^2}{2m} |\vec{G} + \vec{k}|^2 B_{n'\vec{k}'}^{\sigma'} (\vec{G})^* B_{n\vec{k}}^\sigma (\vec{G}),$$

$$\langle n'\vec{k}'\sigma' | \hat{V}_{\text{xtal}} | n\vec{k}\sigma \rangle = \sum_{\vec{G},\vec{G}'} B_{n'\vec{k}'}^{\sigma'} (\vec{G}')^* B_{n\vec{k}}^\sigma (\vec{G}) \sum_{\sigma'',\alpha} V_\alpha^{\sigma''} \left(|\vec{G} + \vec{k} - \vec{G}' - \vec{k}'|^2 \right) W_\alpha^{\sigma''} (\vec{k} - \vec{k}') e^{i(\vec{G} + \vec{k} - \vec{G}' - \vec{k}') \cdot \vec{d}_\alpha^{\sigma''}},$$

$$S_{n'\vec{k}'\sigma',n\vec{k}\sigma} \equiv \langle n'\vec{k}'\sigma' | n\vec{k}\sigma \rangle.$$

Here, the atoms are on regular sites of the underlying Bravais lattice: $\vec{R}_{n_1,n_2,n_3} = n_1\vec{a}_1 + n_2\vec{a}_2 + n_3\vec{a}_3$ where $\{\vec{a}_i\}$ are its direct lattice vectors of the Bravais lattice. Both the NC and the host matrix are assumed to possess the same lattice constant and the whole structure is within a supercell which imposes the periodicity condition $W(\vec{R}_{n_1,n_2,n_3} + N_i\vec{a}_i) = W(\vec{R}_{n_1,n_2,n_3})$, recalling its Fourier representation $W(\vec{R}_{n_1,n_2,n_3}) \rightarrow \sum \tilde{W}(q) e^{i\vec{q} \cdot \vec{R}_{n_1,n_2,n_3}}$, implies $e^{i\vec{q} \cdot N_i\vec{a}_i} = 1$, so that $\vec{q} \rightarrow \vec{q}_{m_1,m_2,m_3} = \vec{b}_1 \frac{m_1}{N_1} + \vec{b}_2 \frac{m_2}{N_2} + \vec{b}_3 \frac{m_3}{N_3}$, where $\{\vec{b}_i\}$ are the reciprocal lattice vectors of the *bulk* material. Thus the reciprocal space of the supercell arrangement is not a continuum but is of the grid form composed of points $\{\vec{q}_{m_1,m_2,m_3}\}$, where $m_i = 0, 1, \dots, N_i - 1$.

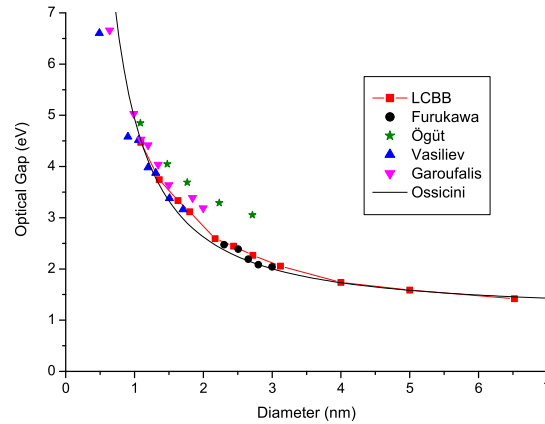


FIG. 9: Comparison of optical gap as a function of Si NC diameter of LCBB results with previous experimental and theoretical data: Furukawa,¹⁰⁰ Ögüt,¹⁰¹ Vasiliev,¹⁰² Garoufalidis,¹⁰³ and the fitting by Ossicini.¹

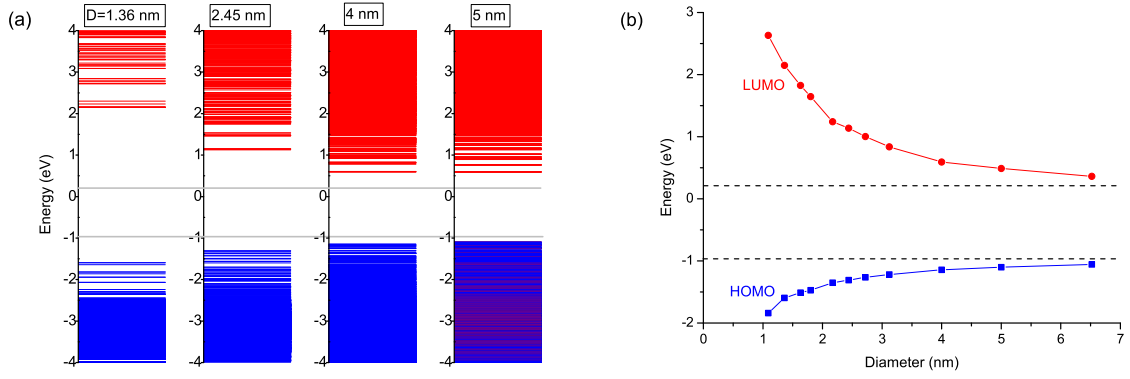


FIG. 10: (a) The evolution of states for four increasing diameters of Si NCs, (b) HOMO and LUMO variation with respect to diameter. The bulk band edges of Si are marked with a dashed line for comparison.

A. Effective optical gap

The hallmark of quantum size effect in NCs has been the widening of the optical gap, as demonstrated by quite a number of theoretical and experimental studies performed within the last decade. Figure 9 contains a compilation of some representative results. For Si NCs, it can be observed that there is a good agreement among the existing data, including LCBB results. In the latter approach, the optical gap directly corresponds to the LUMO-HOMO energy difference, as calculated by the single-particle Hamiltonian in Eq. (5). Such a simplicity relies on the finding of Delerue and coworkers that the self-energy and Coulomb corrections almost exactly cancel each other for Si NCs larger than a diameter of 1.2 nm.⁷² The evolution of the individual states with increasing size is shown in Fig. 10 (a). In particular, the HOMO and LUMO variation is plotted in Fig. 10 (b). It can be clearly observed that for a diameter larger than about 6 nm the quantum size effect essentially disappears.

B. Radiative lifetime

An excellent test for the validity of the electronic structure is through the computation of the direct photon emission. The associated radiative lifetime for the transition between HOMO and LUMO is obtained via time-dependent perturbation theory utilizing the momentum matrix element, which was first undertaken by Dexter.¹⁰⁴ Here, we use the expression offered by Califano *et al.*¹⁰⁵ which differs somewhat in taking into account the local field effects:

$$\frac{1}{\tau_{fi}} = \frac{4}{3} \frac{n}{c^2} F^2 \alpha \omega_{fi}^3 |r_{fi}|^2, \quad (7)$$

where $\alpha = e^2/\hbar c$ is the fine structure constant, $n = \sqrt{\epsilon_{\text{matrix}}}$ is the refractive index of the host matrix, $F = 3\epsilon_{\text{matrix}}/(\epsilon_{\text{NC}} + 2\epsilon_{\text{matrix}})$ is the screening factor within the real-cavity model,¹⁰⁶ ω_i is the angular frequency of the emitted photon, c is the speed of light. Using for the dipole length element between the initial (i) and final states (f), the expression $r_{fi} = \langle f|p|i\rangle/(im_0\omega_{fi})$, we can rewrite the Eq. (7) as,

$$\frac{1}{\tau_{fi}} = \frac{16\pi^2}{3} n F^2 \frac{e^2}{\hbar^2 m_0^2 c^3} (E_f - E_i) |\langle i|p|f\rangle|^2. \quad (8)$$

To obtain the thermally-averaged radiative lifetime, the Boltzmann average is performed over the states close to the HOMO and LUMO as

$$\frac{1}{\langle \tau_r \rangle} = \frac{\sum_{fi} \frac{1}{\tau_{fi}} e^{-\beta(E_{fi} - E_G)}}{\sum_{fi} e^{-\beta(E_{fi} - E_G)}}, \quad (9)$$

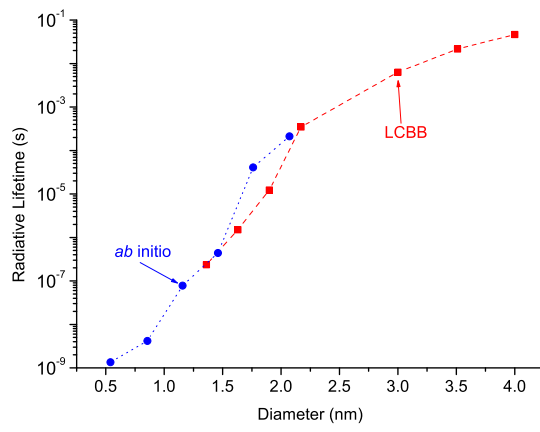


FIG. 11: The variation of the radiative lifetime with respect to diameter for Si NCs.

where E_G is the HOMO-LUMO gap, $\beta = 1/(k_B T)$, and k_B is the Boltzmann constant.

The results¹⁰⁷ for the radiative lifetime in Si NCs as a function of diameter are shown in Fig. 11. The LCBB values for large NCs merge very well with the *ab initio* calculations for small NCs.¹⁰⁸ It should be noted that the radiative lifetime is reduced exponentially, as the NC size is reduced, turning the indirect bandgap bulk materials into efficient light emitters. It needs to be remembered that, the nonradiative processes in Si NCs, Auger recombination and carrier multiplication, are still much more efficient than the radiative process.⁴⁶ As another remark, for larger NCs the level spacings become comparable to phonon energies. Therefore, the direct recombination as considered here, needs to be complemented by the phonon-assisted recombination beyond approximately 3-4 nm diameters.

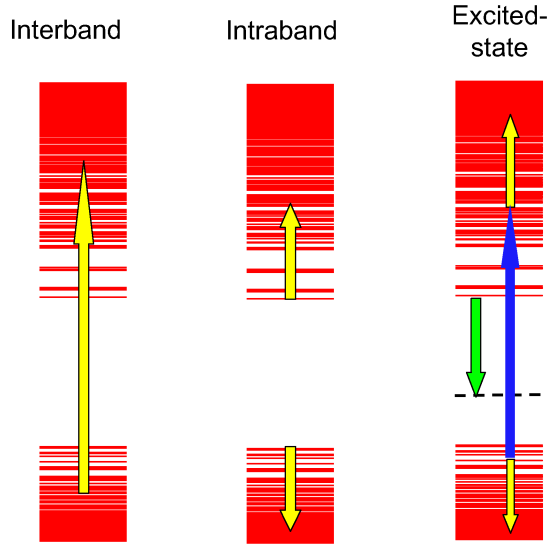


FIG. 12: Illustration for the three different absorption processes in NCs considered here: interband, intraband and excited-state absorption. The yellow (light-colored) arrows indicate the direct photon absorption transitions, the blue (dark-colored) arrow represents optical pumping and the downward green arrow corresponds to luminescence which can be to a interface state (dashed line).

Once the electronic wavefunctions of the NCs are available, their linear optical properties can be readily computed. The three different types of direct photon (zero-phonon) absorption processes are illustrated in Fig. 12. These are interband, intraband and excited-state absorptions. In the latter, the blue (dark-colored) arrow represents optical pumping and following carrier relaxation, the downward green arrow corresponds to luminescence which can be to a final interface state (dashed line).⁶ For all these processes, the relevant quantity is the imaginary part of the dielectric function (which was denoted by ϵ_2 in Sec. II). Within the independent-particle approximation and the artificial supercell framework, it can be put to an alternative form,¹⁰⁹

$$\text{Im}\{\epsilon_{aa}(\omega)\} = \frac{(2\pi e\hbar)^2}{m_0 V_{\text{SC}}} \sum_{c,v} \frac{f_{cv}^{aa}}{E_c - E_v} \frac{\Gamma/(2\pi)}{[E_c - E_v - \hbar\omega]^2 + (\Gamma/2)^2}, \quad (10)$$

where, $a = x, y, z$ denotes the Cartesian components of the dielectric tensor and

$$f_{cv}^{aa} = \frac{2|\langle c|p_a|v\rangle|^2}{m_0(E_c - E_v)}, \quad (11)$$

is the oscillator strength of the transition. In these expressions, e is the magnitude of the electronic charge, and Γ is the full-width at half maximum value of the Lorentzian broadening. The label v (c) correspond to occupied (empty) valence (conduction) states, referring only to their orbital parts in the absence of spin-orbit coupling; the spin summation term is already accounted in the prefactor of Eq. (10). Finally, V_{SC} is the volume of the supercell which is a fixed value, chosen conveniently large to accommodate the NCs of varying diameters. However, if one replaces it with that of the NC, V_{NC} , this corresponds calculating $\text{Im}\{\epsilon_{aa}\}/f_v$, where $f_v = V_{\text{NC}}/V_{\text{SC}}$ is the volume filling ratio of the NC. For the sake of generality, this is the form the results will be presented here. The electromagnetic *intensity* absorption coefficient $\alpha(\omega)$ is related to the imaginary part of the dielectric function through¹¹⁰

$$\text{Im}\{\epsilon_{aa}(\omega)\} = \frac{n_r c}{\omega} \alpha_{aa}(\omega), \quad (12)$$

where n_r is the index of refraction and c is the speed of light.

In the case of intraband absorption, its rate depends on the amount of excited carriers. Therefore, we consider the absorption rate for *one* excited electron or hole that lies at an initial state i with energy E_i . As there are a number of closely spaced such states, we perform a Boltzmann averaging over these states as $e^{-\beta E_i}/\sum_j e^{-\beta E_j}$. We further assume that the final states have no occupancy restriction, which can easily be relaxed if needed. The expression for absorption rate per an excited carrier in each NC becomes

$$\frac{\alpha_{aa}}{f_v} = \frac{\pi e^2}{2m_0 c n_r \omega V_{\text{NC}}} \sum_{i,f} \frac{e^{-\beta E_i}}{\sum_j e^{-\beta E_j}} f_{fi}^{aa} [E_f - E_i] \frac{\Gamma/(2\pi)}{[E_f - E_i - \hbar\omega]^2 + (\Gamma/2)^2}, \quad (13)$$

where again a is the light polarization direction.

Finally, we include the surface polarization effects, also called local field effects (LFE) using a simple semiclassical model, which agrees remarkably well with more rigorous treatments.¹¹¹ We give a brief description of its implementation. First, using the expression

$$\epsilon_{\text{SC}} = f_v \epsilon_{\text{NC}} + (1 - f_v) \epsilon_{\text{matrix}}, \quad (14)$$

we extract (i.e., de-embed) the size-dependent NC dielectric function, ϵ_{NC} , where ϵ_{SC} corresponds to Eq. (10), suppressing the cartesian indices. ϵ_{matrix} is the dielectric function of the host matrix; for simplicity, we set it to the permittivity value of SiO_2 , i.e., $\epsilon_{\text{matrix}} = 4$. Since the wide band-gap matrix introduces no absorption up to an energy of about 9 eV, we can approximate $\text{Im}\{\epsilon_{\text{NC}}\} = \text{Im}\{\epsilon_{\text{SC}}\}/f_v$. One can similarly obtain the $\text{Re}\{\epsilon_{\text{NC}}\}$ within the random-phase approximation,¹¹² hence get the full complex dielectric function ϵ_{NC} . According to the classical Clausius-Mossotti approach, which is shown to work also for NCs,¹¹³ the dielectric function of the NC is modified as

$$\epsilon_{\text{NC,LFE}} = \epsilon_{\text{matrix}} \left[\frac{4\epsilon_{\text{NC}} - \epsilon_{\text{matrix}}}{\epsilon_{\text{NC}} + 2\epsilon_{\text{matrix}}} \right], \quad (15)$$

to account for LFE. The corresponding supercell dielectric function, $\epsilon_{\text{SC,LFE}}$ follows using Eq. (14). Similarly, the intensity absorption coefficients are also modified due to surface polarization effects, cf. Eq. (12).

For applications such as in solar cells, an efficient interband absorption over a certain spectrum is highly desirable. Depending on the diameter, Si NCs possess strong absorption towards the UV region. In Fig. 13 we compare LCBB results⁴⁴ with the experimental data of Wilcoxon *et al.* for Si NCs.¹¹⁴ There is a good overall agreement especially with LFE. The major discrepancies can be attributed to excitonic effects that are not included in the LCBB results. In Fig. 13 we also display the tight binding result of Trani *et al.* which also includes LFE.¹¹¹

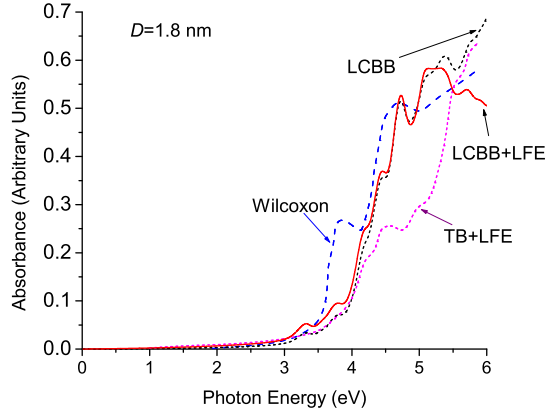


FIG. 13: Comparison of LCBB absorbance results with the available data: experimental work of Wilcoxon *et al.*¹¹⁴ and the theoretical tight binding results of Trani *et al.*¹¹¹ For LCBB spectra, a Lorentzian broadening energy full width of 200 meV is used.

2. Intraband absorption

The electrical injection of carriers or doping opens the channel for intraband absorption, also termed as intersub-band absorption which has practical importance for mid- and near-infrared photodetectors.¹¹⁵ We assume that these introduced carriers eventually relax to their respective band edges and attain a thermal distribution. Therefore, we perform a Boltzmann averaging at room temperature (300 K) over the initial states around LUMO (HOMO) for electrons (holes). The absorption coefficients to be presented are for unity volume filling factors and for one carrier per NC; they can easily be scaled to a different average number of injected carriers and volume filling factors. In Fig. 14 the Si NCs of different diameters are compared.⁴⁴ The intraband absorption is observed to be enhanced as the NC size grows up to about 3 nm followed by a drastic fall for larger sizes. For both holes and electrons very large number of absorption peaks are observed from 0.5 eV to 2 eV. Recently, de Sousa *et al.* have also considered the intraband absorption in Si NCs using the effective mass approximation and taking into account the multi-valley anisotropic band structure of Si.¹¹⁶ However, their absorption spectra lacks much of the features seen in Fig. 14. Mimura *et al.* have measured the optical absorption in heavily phosphorus doped Si NCs of a diameter of 4.7 nm.¹¹⁷ This provides us an opportunity to compare the LCBB results on the intraconduction band absorption in Si NCs. There is a good order-of-magnitude agreement. However, in contrast to LCBB spectra in Fig. 14 which contains well-resolved peaks, they have registered a smooth spectrum which has been attributed by the authors to the smearing out due to size and shape distribution within their NC ensemble.¹¹⁷

3. Excited-state absorption

An optical pumping well above the effective band gap leads to excited-state absorption, also termed as photoinduced absorption, which is an undesired effect that can inhibit the development of optical gain.¹¹⁸ Recent experiments on excited-state absorption concluded that more attention should be devoted to the role of the excitation conditions in the quest for the silicon laser.^{119–121} For this reason, we consider another intraband absorption process where the system is under a continuous interband optical pumping that creates electrons and holes with excess energy. We

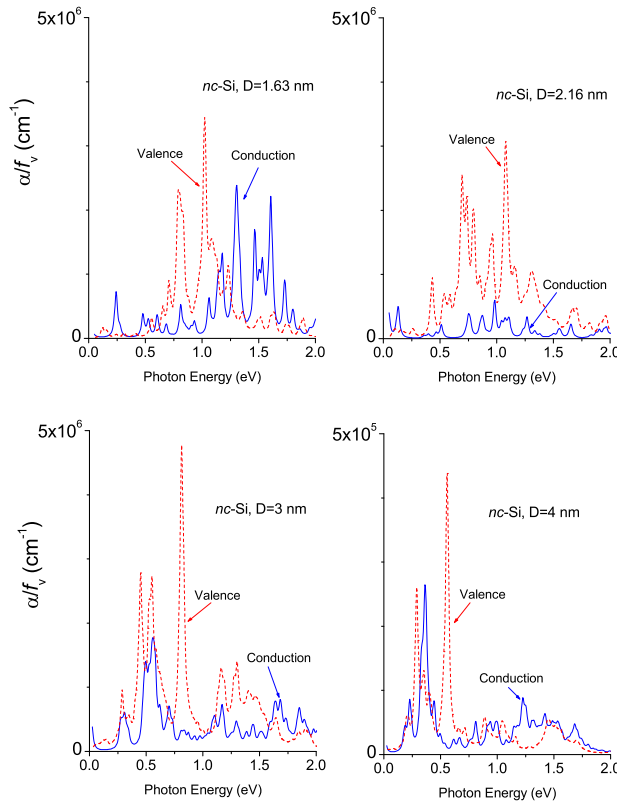


FIG. 14: Intravalence and intraconduction state absorption coefficients in Si NCs of different diameters per excited carrier and at unity filling factor. A Lorentzian broadening energy full width of 30 meV is used. Mind the change in the vertical scale for 4 nm diameter case.

consider three different excitation wavelengths: 532 nm, 355 nm and 266 nm which respectively correspond to the second-, third- and fourth-harmonic of the Nd-YAG laser at 1064 nm. The initial states of the carriers after optical pumping are chosen to be at the pair of states with the maximum oscillator strength among interband transitions under the chosen excitation. As a general trend, it is observed that the excess energy is unevenly partitioned, mainly in favor of the conduction states.^{44,46} Once again a Boltzmann averaging is used to get the contribution of states within the thermal energy neighborhood.

Considering 3 nm and 4 nm diameters, the results⁴⁴ are shown in Fig. 15. Note that the 532 nm excitation results are qualitatively similar to those in intraband absorption, cf. Fig. 14. This is expected on the grounds of small excess energy for this case. Some general trends can be extracted from these results. First of all, the conduction band absorption is in general smooth over a wide energy range. On the other hand the valence band absorption contains pronounced absorption at several narrow energy windows mainly below 1 eV and they get much weaker than the conduction band absorption in the remaining energies. As the excitation energy increases the absorption coefficient per excited carrier in general decreases. In connection to silicon photonics, we should point out that the excited-state absorption is substantial including the important 1.55 μm fiber optics communication wavelength. These results provide a more comprehensive picture than the reported experimental measurements^{119–121} which are usually obtained at a single energy of the probe beam. Finally, it needs to be mentioned that for both intraband and excited-state absorptions displayed in Figs. 14 and 15, the high energy parts will be masked by the interband transition whenever it becomes energetically possible.

D. Third-order nonlinear optical properties

Recent experimental reports show that Si NCs have promising nonlinear optical properties and device applications.^{122–124} One group of very important optical nonlinearities is the third-order nonlinearities which involve

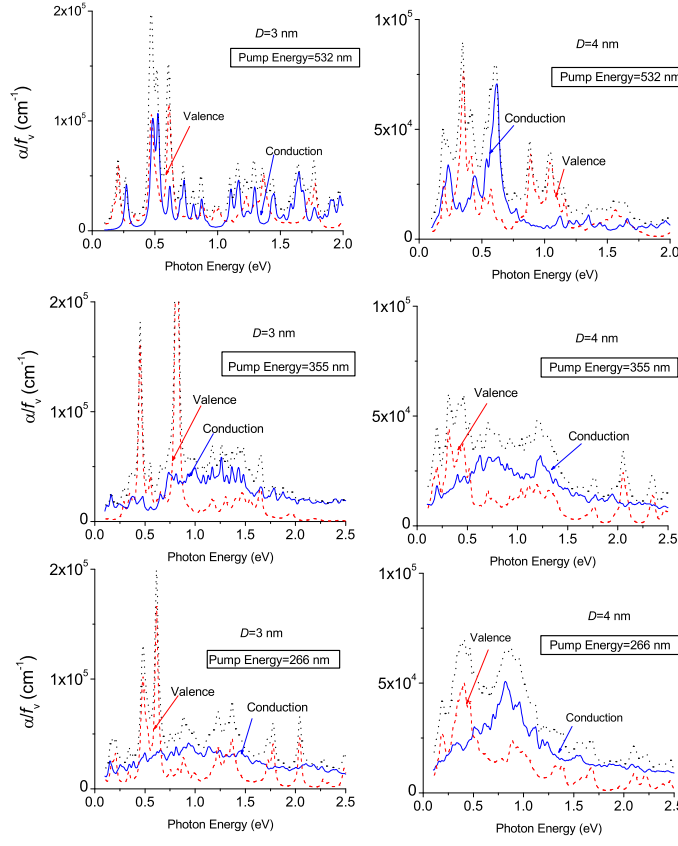


FIG. 15: Excited-state absorption within valence and conduction states of Si NCs per excited carrier and at unity filling factor under three different optical pumping wavelengths of 532 nm, 355 nm and 266 nm. Dotted lines in black color refer to total absorption coefficients. Two different diameters are considered, 3 and 4 nm. A Lorentzian broadening energy full width of 30 meV is used.

nonlinear refraction coefficient or optical Kerr index n_2 and two-photon absorption coefficient β . These nonlinearities are crucial in all-optical switching and sensor protection applications¹²⁵ as well as in the up-conversion of the sub-band-gap light for the possible solar cell applications.¹²⁶ The third-order nonlinear optical susceptibility expression is obtained through perturbation solution of the density matrix equation of motion.¹²⁵ To simplify the notation, in this section we denote the quantities which refer to unity volume filling factor by an overbar. The final expression is given by¹²⁵

$$\begin{aligned} \overline{\chi}_{dcba}^{(3)}(-\omega_3; \omega_\gamma, \omega_\beta, \omega_\alpha) &\equiv \frac{\chi_{dcba}^{(3)}(-\omega_3; \omega_\gamma, \omega_\beta, \omega_\alpha)}{f_v} \\ &= \frac{e^4}{V_{\text{NC}} \hbar^3} \mathbf{S} \sum_{lmnp} \frac{r_{mn}^d}{\omega_{nm} - \omega_3} \left[\frac{r_{nl}^c}{\omega_{lm} - \omega_2} \left(\frac{r_{lp}^b r_{pm}^a f_{mp}}{\omega_{pm} - \omega_1} \right. \right. \\ &\quad \left. \left. - \frac{r_{lp}^a r_{pm}^b f_{pl}}{\omega_{lp} - \omega_1} \right) - \frac{r_{pm}^c}{\omega_{np} - \omega_2} \left(\frac{r_{nl}^b r_{lp}^a f_{pl}}{\omega_{lp} - \omega_1} - \frac{r_{nl}^a r_{lp}^b f_{ln}}{\omega_{nl} - \omega_1} \right) \right], \end{aligned} \quad (16)$$

where the subscripts $\{a, b, c, d\}$ refer to Cartesian indices, $\omega_3 \equiv \omega_\gamma + \omega_\beta + \omega_\alpha$, $\omega_2 \equiv \omega_\beta + \omega_\alpha$, $\omega_1 \equiv \omega_\alpha$ are the input frequencies, \mathbf{r}_{nm} is the matrix element of the position operator between the states n and m , $\hbar\omega_{nm}$ is the difference between energies of these states, \mathbf{S} is the symmetrization operator,¹²⁵ indicating that the following expression should be averaged over the all possible permutations of the pairs (c, ω_γ) , (b, ω_β) , and (a, ω_α) , and finally $f_{nm} \equiv f_n - f_m$ where f_n is the occupancy of the state n . The \mathbf{r}_{nm} is calculated for $m \neq n$ through $\mathbf{r}_{nm} = \frac{\mathbf{p}_{nm}}{im_0\omega_{nm}}$ where \mathbf{p}_{nm} is the momentum matrix element. Hence, after the solution of the electronic structure, the computational machinery

is based on the matrix elements of the standard momentum operator, \mathbf{p} , the calculation of which trivially reduces to simple summations.

The above susceptibility expression is evaluated without any approximation taking into account all transitions within the 7 eV range. This enables a converged spectrum up to the ultraviolet spectrum. In the case of relatively large NCs the number of states falling in this range becomes excessive making the computation quite demanding. For instance, for the 3 nm NC the number of valence and conduction states (without the spin degeneracy) exceed 3000. As another technical detail, the perfect C_{3v} symmetry of the spherical NCs results in an energy spectrum with a large number of degenerate states.⁴⁴ However, this causes numerical problems in the computation of the susceptibility expression given in Eq. (16). This high symmetry problem can be practically removed by introducing two widely separated vacancy sites deep inside the matrix. Their sole effect is to introduce a splitting of the degenerate states by less than 1 meV.

The refractive index and the absorption, in the presence of the nonlinear optical effects become, respectively, $n = n_0 + n_2 I$, $\alpha = \alpha_0 + \beta I$, where n_0 is the linear refractive index, α_0 is the linear absorption coefficient, and I is the intensity of the light. \bar{n}_2 is proportional to $\text{Re}\{\bar{\chi}^{(3)}\}$, and is given by¹²⁷

$$\bar{n}_2(\omega) = \frac{\text{Re}\{\bar{\chi}^{(3)}(-\omega; \omega, -\omega, \omega)\}}{2n_0^2\epsilon_0 c}, \quad (17)$$

where c is the speed of light. Similarly, $\bar{\beta}$ is given by¹²⁷

$$\bar{\beta}(\omega) = \frac{\omega \text{Im}\{\bar{\chi}^{(3)}(-\omega; \omega, -\omega, \omega)\}}{n_0^2\epsilon_0 c^2}, \quad (18)$$

where ω is the angular frequency of the light. Note that Eqs. (17) and (18) are valid only in the case of negligible absorption. The degenerate two-photon absorption cross section $\bar{\sigma}^{(2)}(\omega)$ is given by¹²⁵

$$\bar{\sigma}^{(2)}(\omega) \equiv \frac{\sigma^{(2)}(\omega)}{f_v} = \frac{8\hbar^2\pi^3 e^4}{n_0^2 c^2} \sum_{i,f} \left| \sum_m \frac{\mathbf{r}_{fm}\mathbf{r}_{mi}}{\hbar\omega_{mi} - \hbar\omega - i\hbar\Gamma} \right|^2 \delta(\hbar\omega_{fi} - 2\hbar\omega), \quad (19)$$

where Γ is the inverse of the lifetime; the corresponding full width energy broadening of 100 meV is used throughout. The sum over the intermediate states, m , requires all interband and intraband transitions. As we have mentioned previously, we compute such expressions without any approximation by including all states that contribute to the chosen energy window. Finally, $\bar{\sigma}^{(2)}(\omega)$ and $\bar{\beta}$ are related to each other through $\bar{\beta} = 2\hbar\omega\bar{\sigma}^{(2)}(\omega)$.

The LFEs lead to a correction factor in the third-order nonlinear optical expressions given by,¹²⁸ $L = \left(\frac{3\epsilon_{\text{matrix}}}{\epsilon_{\text{NC}} + 2\epsilon_{\text{matrix}}}\right)^2 \left|\frac{3\epsilon_{\text{matrix}}}{\epsilon_{\text{NC}} + 2\epsilon_{\text{matrix}}}\right|^2$ where ϵ_{matrix} and ϵ_{NC} are the dielectric functions of the host matrix and the NC, respectively. We fix the local field correction at its *static* value, since when the correction factor is a function of the wavelength it brings about unphysical negative absorption regions at high energies.

We consider four different diameters, $D = 1.41, 1.64, 2.16$ and 3 nm. Their energy gap, E_G as determined by the separation between the LUMO and the HOMO energies show the expected quantum size effect.⁴⁴ The \bar{n}_2 is plotted in Fig. 16 which increases with the decreasing NC size for all frequencies.⁴⁵ The smallest diameter gives us the largest \bar{n}_2 . When compared to the n_2 of bulk Si in this energy interval ($\sim 10^{-14}$ cm²/W),^{129–131} calculated NC n_2 is enhanced by as much as ($\sim 10^4 f_v$) for the largest NC. For Si NCs having a diameter of a few nanometers, Prakash *et al.*¹²² have obtained n_2 of the order of $\sim 10^{-11}$ cm²/W which, in order of magnitude, agrees with LCBB results when a typical f_v is assumed for their samples.

In Fig. 17 we have plotted $\bar{\beta}$ against the photon energy.⁴⁵ Peaks at high energies are dominant in the spectrum and $\bar{\beta}$ decreases with the growing NC volume. The obtained β is about $10^5 f_v$ cm/GW for the largest NC at around 1 eV. When compared to the experimental bulk value (1.5 – 2.0 cm/GW measured at around 1 eV),¹²⁹ calculated NC β is scaled by a factor of 300 – 400 f_v times. Prakash *et al.*¹²² have observed β to be between (10¹ – 10² cm/GW) at 1.53 eV which is close to LCBB values provided that f_v is taken into account. This is in full agreement with the findings of Prakash *et al.*¹²²

We should note that $\bar{\beta}$ is nonzero down to static values due to band tailing as mentioned above. Another interesting observation is that the two-photon absorption threshold is distinctly beyond the half band gap value, which becomes more prominent as the NC size increases. This can be explained mainly as the legacy of the NC core medium, silicon which is an indirect band-gap semiconductor. Hence, the HOMO-LUMO dipole transition is very weak especially for relatively large NCs. We think that this is the essence of what is observed also for the two-photon absorption. As the NC size gets smaller, the HOMO-LUMO energy gap approaches to the direct band-gap of bulk silicon, while the HOMO-LUMO dipole transition becomes more effective.

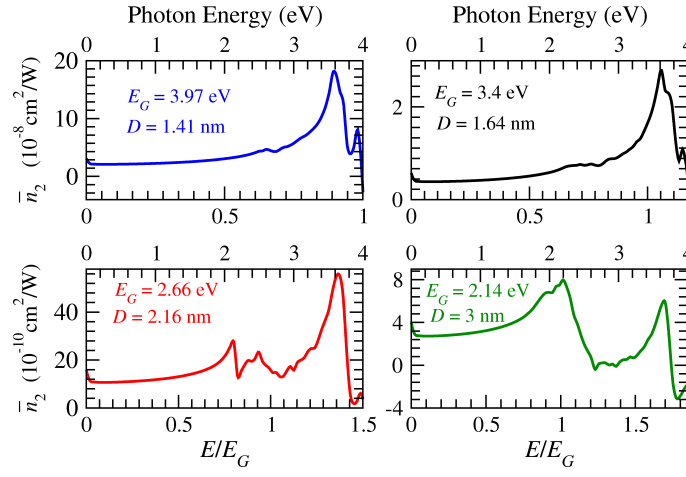


FIG. 16: \bar{n}_2 (i.e., at unity filling) as a function of the photon energy for different NC sizes.

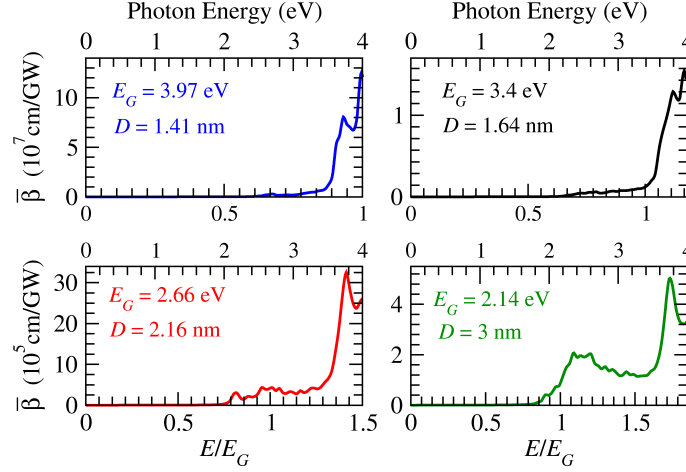


FIG. 17: $\bar{\beta}$ (i.e., at unity filling) as a function of the photon energy for different NC sizes.

E. Quantum-Confined Stark effect in Si Nanocrystals

In 1984, Miller *et al.* discovered a variant of the Stark effect in quantum wells, which was much more robust due to the confinement of the carriers, hence named as the quantum-confined Stark effect (QCSE).¹³² It took more than a decade to observe the same effect in NCs, which were chemically synthesized CdSe colloids.¹³³ Interestingly, it has taken again more than a decade to realize it with Si NCs.¹³⁴ Based on the importance of QCSE for silicon based photonics, in this section we provide a theoretical analysis of QCSE in embedded Si NCs. The basic electrostatic construction of the problem is presented in Fig. 18 with the assumption that the NCs are well separated. If we denote the uniform applied electric field in the matrix region far away from the NC as F_0 , then the solution for electrostatic potential is given in spherical coordinates by¹¹⁰

$$\Phi(r, \theta) = \begin{cases} -\frac{3}{\epsilon+2}F_0r \cos \theta, & r \leq a \\ -F_0r \cos \theta + \left(\frac{\epsilon-1}{\epsilon+2}\right)F_0\frac{a^3}{r^2} \cos \theta, & r > a \end{cases}, \quad (20)$$

where $\epsilon \equiv \epsilon_{\text{NC}}/\epsilon_{\text{matrix}}$ is the ratio of the permittivities of the inside and outside of the NCs. The effect of this external field can be incorporated in the framework of LCBB by adding the $V_{\text{ext}} = e\Phi$ term to the potential energy matrix elements. A computationally convenient approach is to assume that external potential is relatively smooth so that its Fourier transform can be taken to be band-limited to the first Brillouin zone of the underlying unit cell, which leads

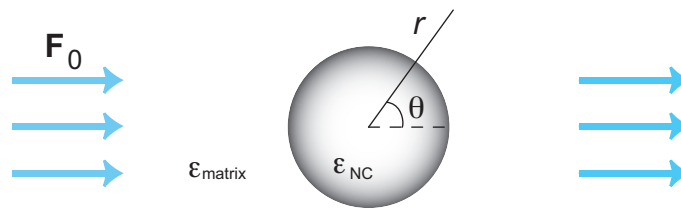


FIG. 18: An illustration for the QCSE showing the geometry and the variables.

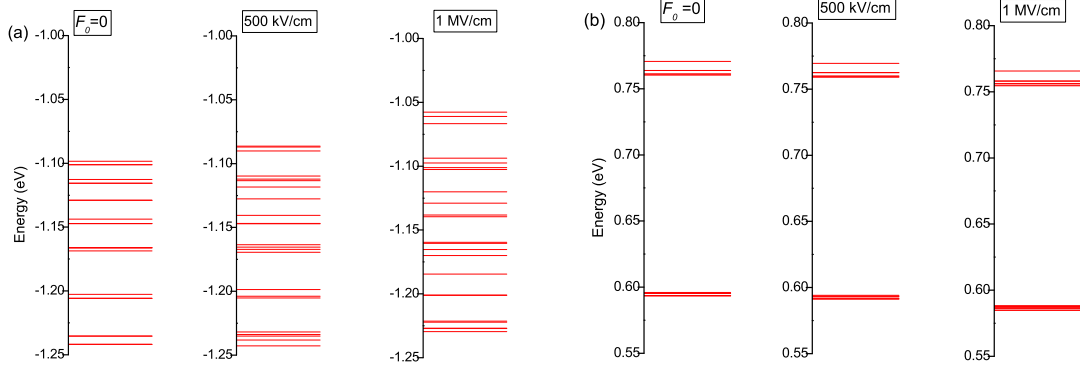


FIG. 19: (a) The Stark shift of the (a) valence, (b) conduction states of a 5 nm-diameter Si NC. The electric field values quoted refer to F_0 , that in the matrix region far away from the NC.

to,⁴²

$$\langle n' \vec{k}' \sigma' | \hat{V}_{\text{ext}} | n \vec{k} \sigma \rangle = \sum_{\vec{G}, \vec{G}'} \text{Rect}_{\vec{b}_1, \vec{b}_2, \vec{b}_3}(\vec{G} + \vec{k} - \vec{G}' - \vec{k}') B_{n' \vec{k}'}^{\sigma'} (\vec{G}')^* B_{n \vec{k}}^{\sigma} (\vec{G}), \quad (21)$$

here $\text{Rect}_{\vec{b}_1, \vec{b}_2, \vec{b}_3}$ is the rectangular pulse function, which yields unity when its argument is within the first Brillouin zone defined by the reciprocal lattice vectors, $\{\vec{b}_1, \vec{b}_2, \vec{b}_3\}$, and zero otherwise.

In Fig. 19 we show the evolution of the valence and conduction states of a 5 nm-diameter Si NC under increasing electric fields. This clearly indicates that valence states are more prone to Stark shift. The LUMO-HOMO band gap Stark shift is plotted in Fig. 20. As in any electronic structure calculation, this is done at 0 K. However, a shift of more than 80 meV points out that the QCSE can be easily measured at room temperature. The dotted line in this figure is a quadratic fit. The deviation for large electric fields indicates the change in charge displacement regime.

Finally, in Fig. 21 the intravalence and intraconduction state electroabsorption curves of a 5 nm-diameter Si NC are shown, under zero and 1 MV/cm electric fields. As expected from the rigidity of the conduction states under the electric field from Fig. 19, the electroabsorption effect can be best utilized in p-doped Si NCs. These results can be important for the assessment of the prospects of nanocrystalline Si-based infrared electroabsorption modulators.

Acknowledgments

The C.B. would like to thank Hasan Yıldırım and Cem Sevik for their valuable contributions. S.O. will thank all the contributors to the publications, that have been important for this work. This work has been supported by the European FP6 Project SEMINANO with the contract number NMP4 CT2004 505285, by the Turkish Scientific and Technical Council TÜBİTAK with the project number 106T048, by MIUR PRIN2007 Italy, and Progetto Italia-

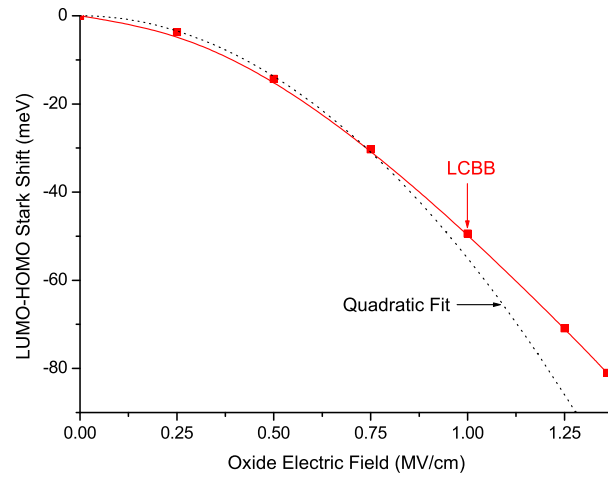


FIG. 20: The LUMO-HOMO band gap Stark shift of a 5 nm-diameter Si NC. The solid line is to guide the eyes.

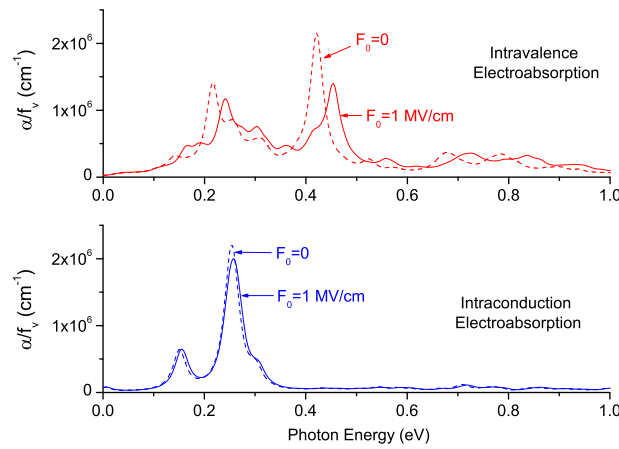


FIG. 21: The intravalence and intraconduction state electroabsorption curves of a 5 nm-diameter Si NC at $T = 300$ K.

Turchia CNR.

-
- ¹ S. Ossicini, L. Pavesi, and F. Priolo, "Light Emitting Silicon for Microphotonics", Springer Tracts on Modern Physics **194** (Springer-Verlag, Berlin, 2003).
 - ² O. Bisi, S. Ossicini, and L. Pavesi, Surf. Sci. Rep. **38**, 5 (2000).
 - ³ B. Geloz, A. Kojima, N. Koshida, Appl. Phys. Lett. **87**, 031107 (2005).
 - ⁴ G. Franz, A. Irrera, E. C. Moreira, M. Miritello, F. Iacona, D. Sanfilippo, G. Di Stefano, P. G. Falica, F. Priolo, Appl. Phys. **A77**, 57 (2003).
 - ⁵ R. J. Walters, G.I. Bourianoff, H.A. Atwater, Nature Materials **4**, 143 (2005).
 - ⁶ L. Pavesi, L. Dal Negro, C. Mazzoleni, G. Franzó, F. Priolo, Nature (London) **408**, 440 (2000).
 - ⁷ L. Khriachtchev, M. Rasanen, S. Novikov, J. Sinkkonen, Appl. Phys. Lett. **79**, 1249 (2001).
 - ⁸ L. Dal Negro, M. Cazzanelli, L. Pavesi, S. Ossicini, D. Pacifici, G. Franzó, F. Priolo, F. Iacona, Appl. Phys. Lett. **82**, 4636 (2003).
 - ⁹ J. Ruan, P. M. Fauchet, L. Dal Negro, M. Cazzanelli, L. Pavesi, Appl. Phys. Lett. **83**, 5479 (2003).
 - ¹⁰ M. Cazzanelli, D. Kovalev, L. Dal Negro, Z. Gaburro, L. Pavesi, Phys. Rev. Lett. **93**, 207042 (2004).

- ¹¹ K. Luterova, K. Dohnalova, V. Servcek, I. Pelant, J.-P. Likforman, O. Crgut, P. Gilliot, B. Hönerlage, Appl. Phys. Lett. **87**, 3280 (2004).
- ¹² L. T. Canham, Appl. Phys. Lett. **57**, 1046 (1990).
- ¹³ "Optical Properties of Low Dimensional Silicon Structures", ed. by D. Bensahel, L. T. Canham, and S. Ossicini, Kluwer, Dordrecht, Amsterdam (1993).
- ¹⁴ B. Hamilton, Semicond. Sci. Technol. **10**, 1187 (1995).
- ¹⁵ Y. Kanemitsu, Phys. Rep. **263**, 1 (1995).
- ¹⁶ G. S. John, and V. A. Singh, Phys. Rep. **263**, 93-151 (1995).
- ¹⁷ "Properties of Porous Silicon", ed. by L. T. Canham, INSPEC: The Institution of Electrical Engineers, London, (1997).
- ¹⁸ A. G. Cullis, L. T. Canham, and P. D. J. Calcott, J. Appl. Phys. **82**, 909 (1997).
- ¹⁹ Y. Takahashi, T. Furuta, Y. Ono, T. Tsushima, and M. Tabe, Jpn. J. Appl. Phys. **34**, 950 (1995).
- ²⁰ D. J. Lockwood, Z. H. Lu, and J. -M. Baribeau, Phys. Rev. Lett. **76**, 539 (1996).
- ²¹ S. V. Novikov, J. Sinkkonen, O. Kilpela, and S. V. Gastev, J. Vac. Sci. Technol. B **15**, 1471 (1997).
- ²² Y. Kanemitsu, and S. Okamoto, Phys. Rev. B **56**, R15561 (1997).
- ²³ V. Mulloni, R. Chierchia, C. Mazzoleni, G. Pucker, L. Pavesi, and P. Bellutti, Phil. Mag. B **80**, 705-718 (2000).
- ²⁴ R. J. Baierle, M. J. Caldas, E. Molinari, and S. Ossicini, Solid State Commun. **102**, 545 (1997).
- ²⁵ M. V. Wolkin, J. Jorne, P. M. Fauchet, G. Allan, and C. Delerue, Phys. Rev. Lett. **82**, 197 (1999).
- ²⁶ A. Puzder, A. J. Williamson, J. C. Grossman, and G. Galli, Phys. Rev. Lett. **88**, 097401 (2002).
- ²⁷ M. Luppi, S. Ossicini, J. Appl. Phys., **94**, 2130 (2003).
- ²⁸ M. Luppi, S. Ossicini, Phys. Rev. B **71**, 035340 (2005).
- ²⁹ M. Luppi, and S. Ossicini, phys. stat. sol. (a). **197**, 251 (2003).
- ³⁰ I. Vasiliev, J. R. Chelikowsky, and R.M. Martin, Phys. Rev. B **65**, 121302(R) (2002).
- ³¹ S. Ossicini, C. Arcangeli, O. Bisi, E. Degoli, M. Luppi, R. Magri, L. Dal Negro, and L. Pavesi in "Towards the first silicon laser" ed. by L. Dal Negro, S. Gaponenko, and L. Pavesi, Nato Science Series vol. 93 (Kluwer Academic Publishers Dordrecht, 2003) pp. 271.
- ³² A. Di Carlo, Semicond. Sci. Technol. **18**, R1 (2003).
- ³³ C. Delerue and M. Lannoo, *Nanostructures: Theory and Modelling*, Springer-Verlag, Berlin, (2004).
- ³⁴ P. Harrison, *Quantum Wells, Wires and Dots*, Second Edition, Wiley, New York, (2005).
- ³⁵ D. M. Wood and A. Zunger, Phys. Rev. B **53**, 7949 (1996).
- ³⁶ L. -W. Wang, A. Franceschetti and A. Zunger, Phys. Rev. Lett. **78**, 2819 (1997).
- ³⁷ L. -W. Wang and A. Zunger, Phys. Rev. B **59**, 15806 (1999).
- ³⁸ D. Ninno, K. B. Wong, M. A. Gell and M. Jaros, Phys. Rev. B **32**, 2700 (1985).
- ³⁹ D. Ninno, M. A. Gell and M. Jaros, J. Phys. C: Solid State Phys. **19**, 3845 (1986).
- ⁴⁰ S. Botti and L. C. Andreani, Phys. Rev. B **63**, 235313 (2001).
- ⁴¹ S. Botti, N. Vast, L. Reining, V. Olevano and L. C. Andreani, Phys. Rev. B **70**, 045301 (2004)
- ⁴² F. Chirico, A. Di Carlo and P. Lugli, Phys. Rev. B **70**, 045314 (2001).
- ⁴³ C. Bulutay, Physica E **38**, 112 (2007).
- ⁴⁴ C. Bulutay, Phys. Rev. B **76**, 205321 (2007).
- ⁴⁵ H. Yildirim and C. Bulutay, Optics Commun. **281**, 4118 (2008); **281**, 6146 (2008).
- ⁴⁶ C. Sevik and C. Bulutay, Phys. Rev. B **77**, 125414 (2008).
- ⁴⁷ First-Principles computation of material properties: The ABINIT software project (URL <http://www.abinit.org>).
- ⁴⁸ A. Puzder, A.J. Williamson, J.C. Grossman, G. Galli, J. Am. Chem. Soc. **125**, 2786 (2003).
- ⁴⁹ A. Franceschetti, S. T. Pantelides, Phys. Rev. B **68**, 033313 (2003).
- ⁵⁰ E. Luppi, E. Degoli, G. Cantele, S. Ossicini, R. Magri, D. Ninno, O. Bisi, O. Pulci, G. Onida, M. Gatti, A. Incze, R. Del Sole, Opt. Mater. **27**, 1008 (2005).
- ⁵¹ E. Degoli, G. Cantele, E. Luppi, R. Magri, D. Ninno, O. Bisi, S. Ossicini, Phys. Rev. B **69**, 155411 (2004).
- ⁵² S. Baroni, A. Dal Corso, S. de Gironcoli, P. Giannozzi, C. Cavazzoni, G. Ballabio, S. Scandolo, G. Chiarotti, P. Focher, A. Pasquarello, K. Laasonen, A. Trave, R. Car, N. Marzari, A. Kokalj, <http://www.pwscf.org/>.
- ⁵³ D. Vanderbilt, Phys. Rev. B **41**, R7892 (1990).
- ⁵⁴ F. Bassani and G. Pastori Parravicini, *Electronic States and Optical Transitions in Solids* (Pergamon Press, New York, 1975).
- ⁵⁵ L. Hedin, Phys. Rev. A **139**, 796 (1965).
- ⁵⁶ G. Onida, L. Reining, and A. Rubio, Rev. Mod. Phys. **74**, 601 (2002) and references therein.
- ⁵⁷ G. Allan, C. Delerue, and M. Lannoo, Phys. Rev. Lett. **76**, 2961 (1996).
- ⁵⁸ U. Itoh, Y. Toyoshima, H. Onuki, N. Washida, T. Ibuki, J. Chem. Phys. **85**, 4867 (1986).
- ⁵⁹ M. Gatti, G. Onida, Phys. Rev. B **72**, 045442 (2005).
- ⁶⁰ The Si₁₀H₁₄ >O cluster we considered here corresponds to the Si₁₀H₁₄O-sym of Ref. 59, where O make a bridge between "second neighbors" Si atoms. We have obtained similar results have for the Si₁₀H₁₄O-asym case, where O is in between two "first neighbors" Si atoms.
- ⁶¹ M. Luppi, S. Ossicini, J. Appl. Phys. **94**, 2130 (2003).
- ⁶² Z. Ma, X. Liao, G. Kong, J. Chu, Appl. Phys. Lett. **75**, 1857 (1999).
- ⁶³ G. Cantele, E. Degoli, E. Luppi, R. Magri, D. Ninno, G. Iadonisi, S. Ossicini, Phys. Rev. B **72**, 113303 (2005).
- ⁶⁴ L. E. Ramos, E. Degoli, G. Cantele, S. Ossicini, D. Ninno, J. Furthmüller, F. Bechstedt, J. Phys.: Cond. Matt. **19**, 466211 (2007).

- ⁶⁵ M. Fujii, Y. Yamaguchi, Y. Takase, K. Ninomiya, and S. Hayashi, Appl. Phys. Lett. **87**, 211919 (2005).
- ⁶⁶ S. Ossicini, E. Degoli, F. Iori, E. Luppi, R. Magri, G. Cantele, F. Trani, and D. Ninno, Appl. Phys. Lett. **87**, 173120 (2005).
- ⁶⁷ L. C. Ciacchi and M. C. Payne, Phys. Rev. Lett. **95**, 196101 (2005).
- ⁶⁸ E. Garrone, F. Geobaldo, P. Rivolo, G. Amato, L. Boarino, M. Chiesa, E. Giamello, R. Gobetto, P. Ugliengo, and A. Vitale, Adv. Mater. (Weinheim, Ger.) **17**, 528 (2005).
- ⁶⁹ EXC Code, V. Olevano, <http://www.bethe-salpeter.org>.
- ⁷⁰ M. Fujii, Y. Yamaguchi, Y. Takase, K. Ninomiya, and S. Hayashi, Appl. Phys. Lett. **85**, 1158 (2004).
- ⁷¹ We have used the non selfconsistent G_0W_0 approach within the RPA plasmon pole approximation. We use a planewave-frequency space code.
- ⁷² C. Delerue, M. Lannoo, and G. Allan, Phys. Rev. Lett. **84**, 2457 (2000).
- ⁷³ C. D. Spataru, S. Ismail-Beigi, L. X. Benedict, and S. G. Louie, Phys. Rev. Lett. **92**, 077402 (2004).
- ⁷⁴ E. Chang, G. Bussi, A. Ruini, and E. Molinari, Phys. Rev. Lett. **92**, 196401 (2004).
- ⁷⁵ E. Luppi, F. Iori, R. Magri, O. Pulci, E. Degoli, S. Ossicini, and V. Olevano, Phys. Rev. B **75**, 033303 (2007).
- ⁷⁶ M. Bruno, M. Palummo, A. Marini, R. Del Sole, V. Olevano, A. N. Kholod, and S. Ossicini, Phys. Rev. B **72**, 153310 (2005).
- ⁷⁷ M. Bruno, M. Palummo, A. Marini, R. Del Sole, and S. Ossicini, Phys. Rev. Lett. **98**, 036807 (2007).
- ⁷⁸ M. Luppi, S. Ossicini, PRB **71**, 035340 (2005).
- ⁷⁹ R. Guerra, R. Magri, L. Martin-Samos, O. Pulci, E. Degoli, S. Ossicini, Superlatt. Microstruct. (2009) in print
- ⁸⁰ H. Kageshima, K. Shiraishi, in: M. Scheffler, R. Zimmermann (Eds.), Proc. 23rd Int. Conf. Phys. Semicon., World Scientific, Singapore, p. 903, (1996).
- ⁸¹ B. W. H. van Beest, G. J. Kramer, R. A. van Santen, Phys. Rev. Lett. **64**, 1955 (1990).
- ⁸² L. Martin-Samos, Y. Limoge, J.-P. Crocombette, G. Roma, E. Anglada, E. Artacho Phys. Rev. B **71**, 014116 (2005).
- ⁸³ P. Ordejón, E. Artacho, J. M. Soler, Phys. Rev. B (Rapid Comm.) **53**, R10441 (1996).
- ⁸⁴ In the last two cases a relaxation run only for the H atoms has been performed before the calculation of the optoelectronic properties.
- ⁸⁵ D. E. Yilmaz, C. Bulutay, T. Çağın, Phys. Rev. B **77**, 155306 (2008).
- ⁸⁶ N. Daldosso, M. Luppi, S. Ossicini, E. Degoli, R. Magri, G. Dalba, P. Fornasini, R. Grisenti, F. Rocca, L. Pavesi, S. Boninelli, F. Priolo, C. Spinella, and F. Iacona, Phys. Rev. B **68**, 085327 (2003).
- ⁸⁷ T. Watanabe, *et al.*, Appl. Surf. Sci. **237**, 125-133 (2004).
- ⁸⁸ G. Hadjisavvas, P.C. Kelires, Physica E **38** 99-105 (2007).
- ⁸⁹ L. Ramos, *et al.*, Appl. Phys. Lett. **87**, 143113 (2005).
- ⁹⁰ L. Ramos, *et al.*, Phys. Rev. B. **71**, 035328 (2005).
- ⁹¹ J. De la Torre, A. Souifi, A. Poncet, G. Bremond, G. Guillot, B. Garrido, J. R. Morante, Solid-State Electronics **49** 1114 (2005).
- ⁹² X. Duan, C. M. Lieber, Adv. Mater. (Weinheim, Ger.) **12**, 298 (2000).
- ⁹³ Y. Kanzawa, T. Kageyama, S. Takeda, M. Fujii, S. Hayashi, K. Yamamoto, Solid State Commun. **102**, 553 (1997).
- ⁹⁴ S. Guha, B. Qadri, R. G. Musket, M. A. Wall, T. Shimizu-Iwayama, J. Appl. Phys. **88**, 3954 (2000).
- ⁹⁵ S. Takeoka, M. Fujii, S. Hayashi, Phys. Rev. B **62**, 16820 (2000).
- ⁹⁶ K. Watanabe, M. Fujii, S. Hayashi, J. Appl. Phys. **90**, 4761 (2001).
- ⁹⁷ E. Lioudakis, A. Antoniou, A. Othonos, C. Christofides, A. G. Nassiopoulou, Ch. B. Lioutas, N. Frangis, J. Appl. Phys. **102** 083534 (2007).
- ⁹⁸ P. Friedel, M. S. Hybertsen, and M. Schlüter, Phys. Rev. B **39**, 7974 (1989).
- ⁹⁹ R. M. Martin, *Electronic Structure*, Cambridge University Press, Cambridge (2004).
- ¹⁰⁰ S. Furukawa, and T. Miyasato, Phys. Rev. B **38**, 5726 (1988).
- ¹⁰¹ S. Ögüt, J. R. Chelikowsky, S. G. Louie, Phys. Rev. Lett. **79**, 1770 (1997).
- ¹⁰² I. Vasiliev, S. Ögüt, and J. R. Chelikowsky, Phys. Rev. Lett. **86**, 1813 (2001).
- ¹⁰³ C. S. Garoufalis, A. D. Zdetsis, and S. Grimme, Phys. Rev. Lett. **87**, 276402 (2001).
- ¹⁰⁴ D. L. Dexter, Solid State Physics (Academic Press Inc., New York), 6, 358 (1958).
- ¹⁰⁵ M. Califano, A. Franceschetti, and A. Zunger, Nano Lett. **5**, 2360 (2005).
- ¹⁰⁶ R. J. Glauber and Lewenstein Phys. Rev. A **43**, 467 (1991).
- ¹⁰⁷ C. Sevik, Ph.D. Thesis, Bilkent University (2008).
- ¹⁰⁸ H.-Ch. Weissker, J. Furthmüller, and F. Bechstedt, Phys. Rev. B **69**, 115310 (2004).
- ¹⁰⁹ H.-Ch. Weissker, J. Furthmüller and F. Bechstedt, Phys. Rev. B **65**, 155327 (2002).
- ¹¹⁰ J. D. Jackson, *Classical Electrodynamics*, 2nd edition, Wiley, New York (1975).
- ¹¹¹ F. Trani, D. Ninno, and G. Iadonisi, Phys. Rev. B **75**, 033312 (2007).
- ¹¹² F. Trani, G. Cantele, D. Ninno, and G. Iadonisi, Phys. Rev. B **72**, 075423 (2005).
- ¹¹³ G. D. Mahan, Phys. Rev. B **74**, 033407 (2006).
- ¹¹⁴ J. P. Wilcoxon, G. A. Samara, and P. N. Provencio, Phys. Rev. B **60**, 2704 (1999).
- ¹¹⁵ V. Ryzhii, I. Khmyrova, V. Mitin, M. Strosio, and M. Willander, Appl. Phys. Lett. **78**, 3523 (2001).
- ¹¹⁶ J. S. de Sousa, J.-P. Leburton, V. N. Freire, and E. F. da Silva Jr., Appl. Phys. Lett. **87**, 031913 (2005).
- ¹¹⁷ A. Mimura, M. Fujii, S. Hayashi, D. Kovalev, and F. Koch, Phys. Rev. B **62**, 12625 (2000).
- ¹¹⁸ A. V. Malko, A. A. Mikhailovsky, M. A. Petruska, J. A. Hollingsworth, and V. I. Klimov, J. Phys. Chem. B **108**, 5250 (2004).

- ¹¹⁹ R. G. Elliman, M. J. Lederer, N. Smith, and B. Luther-Davies, Nuc. Instrum. Methods Phys. Res., Sect. B **206**, 427 (2003).
- ¹²⁰ F. Trojánek, K. Neudert, M. Bittner, and P. Malý, Phys. Rev. B **72**, 075365 (2005).
- ¹²¹ M. Forcales, N. J. Smith, and R. G. Elliman, J. Appl. Phys. B **100**, 014902 (2006).
- ¹²² G.V. Prakash, M. Cazzanelli, Z. Gaburro, L. Pavesi, F. Iacona, F. Franzo, and J.G. Priolo, J. Appl. Phys. **91**, 4607 (2002).
- ¹²³ S.M. King, S. Chaure, J. Doyle, A. Colli, A.C. Ferrari, and W.J. Blau, Opt. Commun. **276**, 305 (2007).
- ¹²⁴ G. S. He, Q. Zheng, K.-T. Yong, F. Erogbogbo, M. T. Swihart, and P. N. Prasad Nano Lett. **8**, 2688 (2008).
- ¹²⁵ R.W. Boyd, Nonlinear Optics, Academic Press, San Diego, 2003.
- ¹²⁶ T. Thürpke, M.A. Green, and P. Würfel, J. Appl. Phys. **92**, 4117 (2002).
- ¹²⁷ M. Sheik-Bahae, A.A. Said, T.H. Wei, D.J. Hagan, and E.W. Van Stryland, IEEE J. Quantum Electron. **26**, 760 (1990).
- ¹²⁸ J.E. Sipe and R.W. Boyd, Optical Properties of Nanostructured Random Media, in: V. M. Shalev (Ed.), Topics Appl. Phys., vol. 82, Springer, Berlin-Heidelberg, 2002.
- ¹²⁹ A.D. Bristow, N. Rotenberg, and H.M. van Driel, Appl. Phys. Lett. **90**, 191104 (2007)
- ¹³⁰ Q. Lin, J. Zhang, G. Piredda, R.W. Boyd, P.M. Fauchet, and G.P. Agrawal, Appl. Phys. Lett. **91**, 021111 (2007).
- ¹³¹ M. Dinu, F. Quochi, and H. Garcia, Appl. Phys. Lett. **82**, 2954 (2003).
- ¹³² D. A. B. Miller, D. S. Chemla, T. C. Damen, A. C. Gossard, W. Wiegmann, T. H. Wood and C. A. Burrus, Phys. Rev. Lett. **53**, 2173 (1984).
- ¹³³ S. A. Empedocles and M. G. Bawendi, Science **278**, 2114 (1997).
- ¹³⁴ M. Kulakci, U. Serincan, R. Turan, and T. G. Finstad, Nanotechnology **19** 455403 (2008) and references therein.